

Ambient Electrosynthesis toward Single-Atom Sites for Electrocatalytic Green Hydrogen Cycling

Xin Zhao, Daping He, Bao Yu Xia, Yujie Sun, and Bo You*

With the ultimate atomic utilization, well-defined configuration of active sites and unique electronic properties, catalysts with single-atom sites (SASs) exhibit appealing performance for electrocatalytic green hydrogen generation from water splitting and further utilization via hydrogen–oxygen fuel cells, such that a vast majority of synthetic strategies toward SAS-based catalysts (SASCs) are exploited. In particular, room-temperature electrosynthesis under atmospheric pressure offers a novel, safe, and effective route to access SASs. Herein, the recent progress in ambient electrosynthesis toward SASs for electrocatalytic sustainable hydrogen generation and utilization, and future opportunities are discussed. A systematic summary is started on three kinds of ambient electrochemically synthetic routes for SASs, including electrochemical etching (ECE), direct electrodeposition (DED), and electrochemical leaching–redeposition (ELR), associated with advanced characterization techniques. Next, their electrocatalytic applications for hydrogen energy conversion including hydrogen evolution reaction, oxygen evolution reaction, overall water splitting, and oxygen reduction reaction are reviewed. Finally, a brief conclusion and remarks on future challenges regarding further development of ambient electrosynthesis of high-performance and cost-effective SASCs for many other electrocatalytic applications are presented.

1. Introduction

The rapid growth of the world's population and the high-speed development of human society result in high energy demand, in which about 85% is currently supplied by nonrenewable fossil fuels including coal, oil, natural gas, and so on.^[1] However, the


usage of fossil fuels with limited reserves not only poses potential energy shortage in the future, but also gives rise to environmental issues like greenhouse effect, acid rain, ozone depletion, and desertification.^[2–4] It is therefore extremely urgent to explore sustainable energy resources with high energy density and environmental benignity to gradually replace fossil fuels in the coming decades.^[5–7] In this regard, hydrogen has been regarded as a promising alternative due to its high heat value and clean combustion.^[8] In fact, since its first proposal by several pioneers, including John Bockris and John Burdon Sanderson Haldane, a novel and clean energy paradigm based on hydrogen, termed as the hydrogen economy, has received much attention.^[9–11] Energy from renewable sources like solar and wind is first stored in the chemical bond of H₂ via (photo)electrochemical water splitting, and can then be released on demand through the reverse reaction in H₂–O₂ fuel cells to close the hydrogen cycle without any pollutant(s) emission (Figure 1).^[12,13] Compared with brown and blue hydrogen generation from steam methane reforming and coal gasification, which consume fossil fuels and cause environmental pollution/CO₂ emission,^[14,15] water splitting to hydrogen possesses obvious advantages, and the resulting hydrogen is thereby considered as green hydrogen.^[12,16–18] To achieve large-scale commercialization of the hydrogen economy, one of the main obstacles that needs to be overcome is the high overpotentials (i.e., low activity) associated with the hydrogen evolution reaction/oxygen evolution reaction (HER/OER) during water splitting and oxygen reduction reaction/hydrogen oxidation reaction (ORR/HOR) in H₂–O₂ fuel cells, which result in low energy conversion efficiencies.^[19–22] Thus, leveraging these advances requires efficient synthetic methods toward high-performance and cost-effective electrocatalysts to accelerate the sluggish kinetics of the involved reactions.

Considering the surface/interface reactive properties during green hydrogen cycling,^[23,24] reducing the size of electrocatalysts to increase their accessible surface area is a simple and straightforward method to promote the specific activities of the underlying electrocatalysts.^[25,26] The extreme along this direction is downsizing to atomic level to obtain single-atom sites-based catalysts (SASCs), such that the maximum atom-utilization efficiency can be achieved.^[27–30] Besides, heterogeneous SASCs with well-defined and uniform configuration of

X. Zhao, D. He
School of Science
Wuhan University of Technology
Wuhan, Hubei 430070, China

B. Y. Xia, B. You
Key Laboratory of Material Chemistry for Energy Conversion and Storage
Ministry of Education
Hubei Key Laboratory of Material Chemistry and Service Failure
School of Chemistry and Chemical Engineering
Huazhong University of Science and Technology
Wuhan, Hubei 430074, China
E-mail: youbo@hust.edu.cn

Y. Sun
Department of Chemistry
University of Cincinnati
Cincinnati, OH 45221, USA

 The ORCID identification number(s) for the author(s) of this article can be found under <https://doi.org/10.1002/adma.202210703>.

DOI: 10.1002/adma.202210703

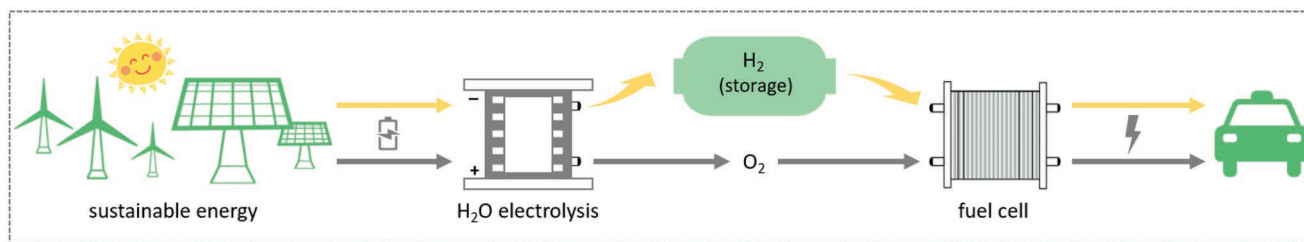


Figure 1. Schematics of hydrogen economy that contains green hydrogen generation from sustainable energy-driven water splitting and conversion to electricity through fuel cells.

active sites inherit the advantages of homogeneous catalysts, providing an ideal platform to explore the structure–activity correlations.^[31–35] Nowadays, single-atom electrocatalysis has become one of the most appealing research frontiers in the field of heterogeneous electrochemistry for energy conversion beyond green hydrogen cycling, including CO₂ reduction,^[36–40] NO₃[−] reduction,^[41–43] N₂ fixation,^[44–46] and biomass upgrading.^[47–50] With the rapid development of nanoscience and the advanced physicochemical characterization techniques such as aberration-corrected high-angle annular dark-field scanning transmission electron microscopy (AC-HAADF-STEM) and synchrotron radiation X-ray absorption spectroscopy (XAS), various synthetic methods have been reported to be effective to obtain SASCs, such as high-temperature atom trapping,^[51–53] high-temperature thermal emission,^[54,55] atomic-layer deposition,^[56–59] photochemical deposition,^[60–62] ultrasonication pulling,^[63] microwave irradiation,^[64,65] mechanical ball milling,^[66] and so on. However, these methods often need either high energy inputs, complex procedures, or expensive equipments with harsh physicochemical conditions. In contrast, ambient electrochemical synthesis can be conducted at room temperature and atmospheric pressure using an electrochemical workstation and the whole preparation processes can usually be finished within a short time.^[67] Moreover, the resulting materials can be directly employed as catalytic electrodes without the requirement of polymeric binders, hence simplifying the electrode preparation process.

Herein, we focus on recent progress in ambient electrocatalysis toward SASCs ranging from nonprecious metals such as Fe, Co, Ni, Cu, Zn, V, Cr, Mn, Sn, Pb, and Bi to noble metals including Ru, Rh, Pd, Ag, Ir, Pt, and Au. Three synthetic strategies including electrochemical etching (ECE), direct electrodeposition (DED), and electrochemical leaching–redeposition (ELR) are presented. Subsequently, the electrocatalytic applications for green hydrogen cycling including HER, OER, overall water splitting (OWS) and ORR electrocatalysis will be discussed as well. The critical challenges and opportunities for future development in this ambient electrocatalysis toward SASCs for diverse electrocatalysis are included finally.

2. Comparison of Synthetic Methods toward SASCs

The successful synthesis of stable catalysts with SASCs is a prerequisite for scientific research and practical applications. It's known that downsizing of metals leads to increased surface energy, which accounts for the aggregation from individual

single atoms to clusters and nanoparticles during synthesis and catalysis processes. It is thus imperative to construct strong interactions between metal single atoms and the surrounding coordination atoms in supports to overcome the aggregation trends for stabilizing SASCs. In general, if the interaction of metal–support is stronger than that of metal–metal, stable SASCs can be obtained. With this in mind, various synthesis strategies toward SASCs have been reported. Due to space limitations, only three typical high-temperature synthetic strategies including atom trapping, thermal emission, and atomic-layer deposition, and two ambient synthesis methods of photochemical reduction and ultrasonication pulling are discussed and compared with ambient electrocatalysis on the basis of recent advances (Figure 2).

Atom trapping is a high-temperature top-down strategy that converts nanoparticulate metals to mobile metal species, which are then trapped by appropriate supports through strong metal–support interaction to form stable SASCs. Figure 2a schematically shows a typical atom-trapping route to prepare thermally stable single-atom Pt trapped by defect CeO₂, as reported by Datye and co-workers.^[51] Different from the obvious Pt sintering for Pt nanoparticles (NPs) on a La–Al₂O₃ support via direct annealing at 800 °C in flowing air, premixing defect CeO₂ results in the migration of Pt NPs from Al₂O₃ to CeO₂ with atomic dispersion due to their strong binding. It can be seen that high temperature to generate mobile metal species and suitable supports that can trap and stabilize these mobile species are two key prerequisites. Although this method avoids the use of expensive equipment, the high-temperature treatments inevitably lead to high energy consumption, which is not environmentally friendly. Moreover, only selected metals at nanoscale and supports featuring strong interaction can be used, limiting its universality and scalability for other metallic SASCs across the periodic table. Another high-temperature top-down strategy toward SASCs is thermal emission (Figure 2b), which uses hot NH₃ gas to haul out bulk metals to emit volatile metal–NH₃ species due to their strong Lewis acid–base interaction, which subsequently migrate to and then anchor on substrates to form SASCs. A typical example is depicted in Figure 2b, Wu's group put commercially available Cu foam and ZIF-8 powder separately in two porcelain boats, which were then subjected to annealing at 900 °C under Ar for converting ZIF-8 to porous N-doped carbon (NC) with abundant defect sites followed by further annealing under NH₃.^[54] Benefitting from the strong Lewis acid–base interaction between Cu and NH₃, Cu atoms were hauled out from the Cu foam to form volatile Cu(NH₃)_x species which finally migrated and

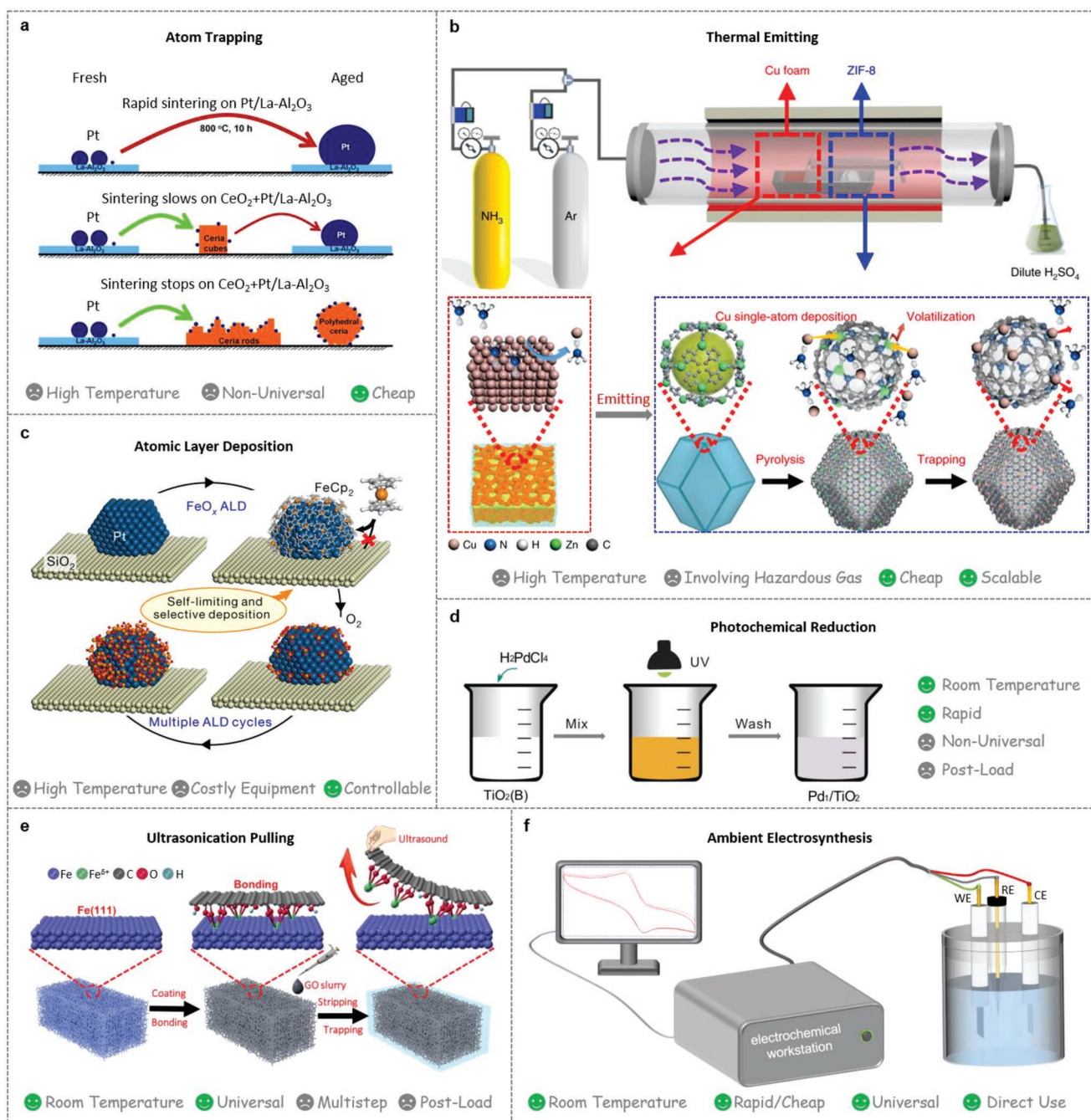


Figure 2. Scheme of various synthesis methods toward SACs and their pros and cons including atom trapping strategy (a), thermal emission (b), atomic-layer deposition (c), photochemical reduction (d), ultrasonication pulling (e), and ambient electrosynthesis (f). a) Reproduced with permission.^[51] Copyright 2016, American Association for the Advancement of Science. b) Reproduced with permission.^[54] Copyright 2018, The Authors, published by Springer Nature. c) Reproduced with permission.^[56] Copyright 2019, Springer Nature. d) Reproduced with permission.^[60] Copyright 2016, American Association for the Advancement of Science. e) Reproduced with permission.^[63] Copyright 2019, Wiley-VCH.

became trapped by the NC substrate to yield Cu single atoms supported on N–C (Cu-SAs/NC). The thermal emission avoids the use of expensive equipment as well, and the easy availability of bulk metal materials renders this strategy potential scalability. While the employment of high temperature and corrosive atmosphere is neither environmentally friendly nor operationally safe. Atomic-layer deposition (ALD) is a chemical gas-phase

deposition method where gaseous precursors are introduced into the surface of the substrate to form the desired SASs via self-limiting surface chemical reactions under elevated temperature. Lu and co-workers reported the atomic dispersion of iron hydroxide ($\text{Fe}_1(\text{OH})_x$) over SiO_2 -supported Pt NPs (Pt/SnO_2) by ALD (Figure 2c).^[56] By alternatively exposing the Pt/SnO_2 sample to ferrocene (FeCp_2) and O_2 atmosphere at a relatively

low temperature (100 °C), the deposition ratio of iron hydroxide on Pt NPs can be decreased which ensures the atomic dispersion. Moreover, the coverage of $\text{Fe}_1(\text{OH})_x$ on Pt NPs can be precisely controlled by multiple ALD cycles. The ALD provides a controllable route to yield SASs, while costly equipment and sophisticated operation are usually needed for accurate tuning of reaction parameters like gas channels, vacuum system, and so on. Also, elevated temperature is commonly necessary.

Relative to the abovementioned high-temperature synthesis, strategies capable of yielding SASs under room temperature would be desirable. Typically, photochemical reduction (Figure 2d) and ultrasonication pulling (Figure 2e) are two ambient synthetic routes toward SASs. For example, Zheng's group used the photochemical reduction method to fabricate atomically dispersed Pd on ethylene glycolate (EG)-stabilized ultrathin TiO_2 nanosheets (Pd_1/TiO_2) under ultraviolet (UV) light irradiation (Figure 2d).^[60] The H_2PdCl_4 was premixed with as-prepared TiO_2 (B) nanosheets to allow sufficient adsorption of Pd species. The resulting mixture was then irradiated by a Xe lamp with low-density UV light for 10 min to obtain Pd_1/TiO_2 after washing with water. The authors confirmed that the EG radicals on TiO_2 nanosheets induced by UV light play a critical role, which facilitates the removal of Cl^- on Pd and stabilizes individual Pd atoms via forming more Pd—O bonds. Although this photochemical reduction is simple and time-saving, it is difficult for it to be extended to fabricate other SASs on diverse substrates especially conductive supports. Recently, Wu's group found that ultrasonication of the graphene oxide (GO)-adsorbed metal foam (Fe, Co, Ni, and Cu) can pull out the metal atoms to obtain metal single atoms/GO hybrids due to their strong bonding with the dangling oxygen atoms in GO (Figure 2e).^[63] This strategy is benign and universal to access a series of SASs on GO, while trivial steps like time-consuming drying process and Ar flowing are required.

In contrast, ambient electrosynthesis can be conducted at room temperature/atmospheric pressure, with only a simple electrochemical workstation needed, and the whole preparation processes can usually be finished within a short time (Figure 2f). By simply adjusting the electrochemical parameters/methods and choosing the appropriate precursors and substrates, a variety of metal-based SASs across the periodic table can be acquired with great precision. Moreover, the resulting materials can be directly used as catalytic electrodes without

any post-treatments like binding with conductive polymeric glues, for example Nafion. These superiorities render such an approach extremely suitable for the preparation of SASCs for many electrocatalytic applications.

3. Ambient Electrosynthesis toward SASs

In fact, electrochemical synthesis of inorganic components can date back to 1807, when Humphry Davy first discovered that alkali metals such as potassium and sodium can be obtained from molten salts by passing an electric current.^[68] Benefiting from the exceptional features, including mild reaction conditions, short synthetic time, cheap instrument requirements, potential universality, and so on (Figure 2f), ambient electrosynthesis is rapidly developing as a promising synthesis technology for a variety of materials including SASCs.^[69–71] Based on the detailed procedures to access SASs, ambient electrosynthesis can be classified into three categories (Figure 3): i) electrochemical etching (ECE), a top-down method to anodically etch the bulk metals away to leave SASs; ii) direct electrodeposition (DED), a bottom-up route to acquire SASs from the corresponding metal-ion precursors in electrolytes, and iii) electrochemical leaching–re-deposition (ELR), a combined top-down and bottom-up approach that anodically leaches bulk metals into electrolytes followed by cathodic deposition to obtain SASs. With these methods, various catalysts with SASs of Fe, Co, Ni, Cu, Zn, V, Cr, Mn, Sn, Pb, Bi, Ru, Rh, Pd, Ag, Ir, Pt, and Au can be prepared. Table 1 shows an overview about their electrosynthesis and the corresponding electrocatalytic activities for various reactions involved in green hydrogen cycling. The detailed electrochemically synthetic parameters can be found in Table S1 in the Supporting Information.

3.1. Electrochemical Etching (ECE)

As discussed above, the electrochemical etching (ECE) is a top-down route that gradually etches bulk metal counterparts away and finally leaves the SASs. For example, Yao and co-workers experimentally showed the successful preparation of Ni single atoms anchored on graphitized carbon (A-Ni-C) via electrochemical etching of the graphene-encapsulated Ni nanoparticles

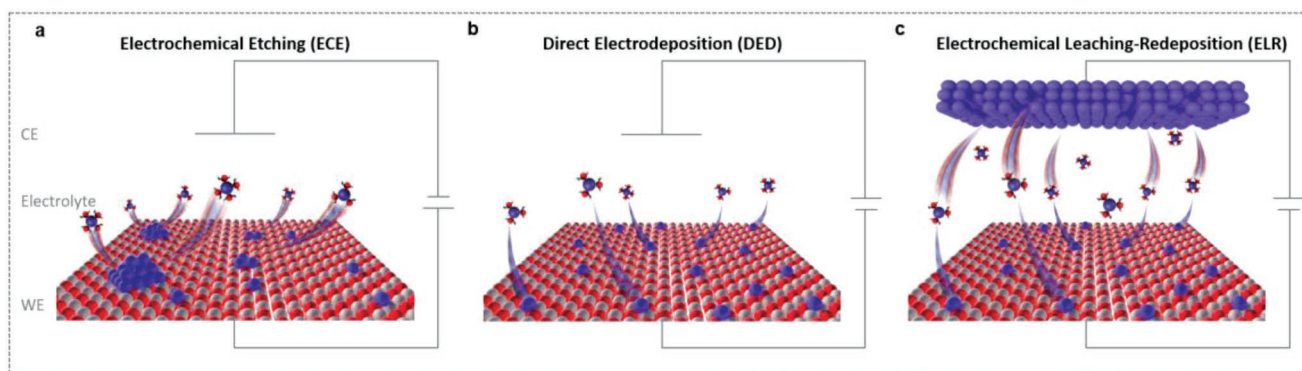


Figure 3. a–c) Schematics of three ambient electrosynthesis strategies toward SASs including electrochemical etching (ECE) (a), direct electrodeposition (DED) (b), and electrochemical leaching–re-deposition (ELR) (c).

Table 1. Summary of ambient electrosynthesis of various single-atom sites catalysts (SASCs) and the electrocatalytic activities for green hydrogen cycling.

Catalyst	Method ^{a)}	Metal precursor	Medium	Substrate	Metal loading	Application	Electrolyte	η_{10}	Reference
A-Ni-C	ECE ^{b)}	Ni@C	0.5 M H ₂ SO ₄	Ni@C	1.5 wt%	HER	0.5 M H ₂ SO ₄	34 mV	[72]
Pt SAs/Bi	DED ^{c)}	150 × 10 ⁻¹⁵ M H ₂ PtCl ₆	Ultrapure H ₂ O	Bi UME		HER	0.5 M NaClO ₄ 40 × 10 ⁻³ M HClO ₄		[74]
Pt _{5A} -NiO/Ni		50 × 10 ⁻⁶ M H ₂ PtCl ₆	1.0 M KOH	NiO/Ni	1.14 wt%	HER	1.0 M KOH	26 mV	[76]
⁵ Au/NiFe LDH		0.3 × 10 ⁻³ M HAuCl ₄	50 × 10 ⁻³ M NaCl	NiFe LDH	0.4 wt%	OER	1.0 M KOH	237 mV	[77]
C/A-Ir ₁ /Co _{0.8} Fe _{0.2} Se ₂		100 × 10 ⁻⁶ M IrCl ₄	1.0 M KOH	Co _{0.8} Fe _{0.2} Se ₂	2.3/1.8 wt%	OWS	1.0 M KOH	1.48 V	[78]
Ir ₁ /NFS		50 × 10 ⁻⁶ M IrCl ₃	1.0 M KOH	Ni _(3-x) Fe _x S ₂	0.6 wt%	OER	1.0 M KOH	170 mV	[79]
Ir-NiCoLDH		45 × 10 ⁻⁶ M H ₂ IrCl ₆	0.1 M Ni(NO ₃) ₂ , 0.1 M Co(NO ₃) ₂	NiCo LDH	0.41 wt%	OER	0.5 M H ₂ SO ₄	240 mV	[80]
Ru ₁ /D-NiFe LDH		0.01–0.06 M RuCl ₃	120 × 10 ⁻³ M Ni(NO ₃) ₂ , 120 × 10 ⁻³ M Fe(NO ₃) ₃ , 1 × 10 ⁻³ M Al(NO ₃) ₃	NiFeAl LDH	1.2 wt%	OWS	1.0 M KOH	1.44 V	[81]
Ni/GD		5 × 10 ⁻³ M NiSO ₄	0.5 M H ₂ SO ₄	GD foam	0.278 wt%	HER	0.5 M H ₂ SO ₄	88 mV	[82]
Fe/GD		10 × 10 ⁻³ M FeCl ₃	0.5 M H ₂ SO ₄	GD foam	0.68 wt%	HER	0.5 M H ₂ SO ₄	66 mV	[82]
Pt-SAs/MoS ₂		5 × 10 ⁻³ M K ₂ PtCl ₄	0.05 M H ₂ SO ₄	Ce-MoS ₂	5.1 wt%	HER	0.5 M H ₂ SO ₄	59 mV	[83]
Co ₁ O _x		900 × 10 ⁻¹⁵ M Co(NO ₃) ₂	0.1 M PBS	C UME		OER	0.2 M NaClO ₄ 10 × 10 ⁻³ M NaOH	>320 mV	[84]
Fe ₁ (OH) _x /P-C		100 × 10 ⁻⁶ M FeCl ₃	1.0 M KOH	P-C	0.72 wt%	OER	1.0 M KOH	320 mV	[85]
SWNT/at-Pt	ELR ^{d)}	Pt foil	0.5 M H ₂ SO ₄	SWNT	0.06 wt%	HER	0.5 M H ₂ SO ₄	40 mV	[86]
PtSA-NT-NF		Pt foil	1 M PBS	NT-NF	1.6 wt%	HER	1.0 M PBS	24 mV	[87]
Mo ₂ TiC ₂ T _x -Pt _{5A}		Pt foil	0.5 M H ₂ SO ₄	Mo ₂ TiC ₂ T _x	1.2 wt%	OER	1.0 M KOH	320 mV	[88]
Pt SA-MoS ₂		Pt foil	0.5 M H ₂ SO ₄	2H-MoS ₂	1.1 at%	HER	0.5 M H ₂ SO ₄	310 mV	[90]
Pt/np-Co _{0.85} Se		Pt foil	0.5 M H ₂ SO ₄	np-Co _{0.85} Se	1.03 wt%	HER	1.0 M PBS	55 mV	[91]
Pt-SAs/C		Pt foil	0.5 M H ₂ SO ₄	Graphite CP	1.26 wt%	HER	0.5 M H ₂ SO ₄	38 mV	[92]
A-CoPt-NC		Co-NC Pt wire	0.5 M H ₂ SO ₄	Co-NC	1.72 _{Co} /0.16 _{Pt} wt%	ORR	0.1 M KOH	270 mV ^{e)}	[93]

^{a)}Detailed synthesis parameters are included in Table S1 in the Supporting Information; ^{b)}ECE: electrochemical etching; ^{c)}DED: direct electrodeposition; ^{d)}ELR: electrochemical leaching–re-deposition; ^{e)}The difference between half-wave and thermodynamic potentials.

(Ni@C) derived from a Ni-based metal-organic framework (Ni-MOF, **Figure 4a–c**).^[72] To be more specific, the Ni@C was subjected to hydrochloric acid (HCl) leaching to remove redundant metallic Ni (Figure 4a). Then, the resulting HCl-leached Ni@C (HCl-Ni@C) was loaded on a glassy carbon electrode (GCE) and cyclic voltammetry (CV) at a scan rate of 100 mV s⁻¹ between -95 and 905 mV versus reversible hydrogen electrode (RHE) was applied for electrochemical etching in 0.5 M H₂SO₄ electrolyte (Figure 4b,c). With consecutive CV scanning, both the reduction current (Figure 4b) and the anodic peak at around 0 V vs RHE increased progressively (Figure 4c), implying gradual Ni etching and activation of the HCl-Ni@C. The negative shift of the anodic peak suggested a more easily oxidative etching. After 4000 cycles, the oxidation peak levelled out and the cathodic current remained stable, indicative of complete etching. To track the entire procedure, the authors conducted a series of physicochemical characterizations including X-ray diffraction (XRD), HAADF-STEM, and elemental analysis. As shown in Figure 4d, the XRD patterns demonstrated that the peak intensities of metallic Ni in HCl-Ni@C relative to Ni@C decrease significantly, suggesting the effective removal of metallic Ni by HCl. After further electrochemical etching,

the disappeared diffraction peaks of metallic Ni in A-Ni@C evidenced the absence of Ni metals. Inductively coupled plasma atomic emission spectroscopy (ICP-AES) disclosed that the weight ratios of Ni are 85.0%, 5.3%, and 1.5% for Ni@C, HCl-Ni@C and A-Ni-C, respectively, verifying the effective removal of Ni by chemical (HCl) and electrochemical (CV) etching. With the assistance of high-resolution TEM and HAADF-STEM, the authors further studied the structural changes of the electrocatalysts before and after electrochemical etching. Clearly observable lattice spacings of 0.204 and 0.176 nm corresponding to the Ni(111) and Ni(200) planes, respectively, confirmed the existence of crystalline Ni metals in HCl-Ni@C. In contrast, HAADF-STEM identified that about 78% of the Ni species are isolated single atoms for A-Ni-C after electrochemical etching, plus a few sub-nanometer clusters.

Recently, Li and co-workers theoretically confirmed the ECE as a general route to produce multiple metallic SAs or clusters like Pt, Pd, and Ni anchored on diverse substrates (e.g., N-doped graphene, Fe₂O₃, and graphdiyne) due to the existence of an electrochemical potential window (ECPW) for a specific material, within which only the single atoms (SAs) bound on the substrate would remain in place while all other aggregated

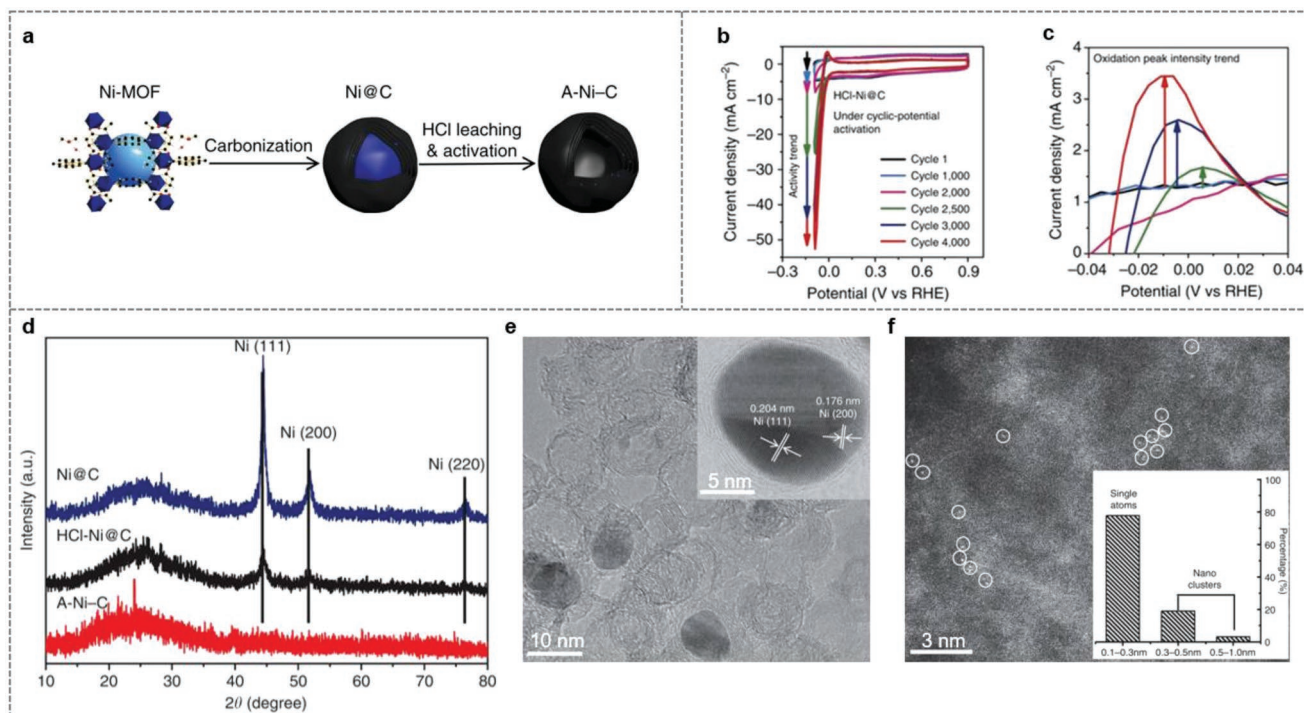


Figure 4. a) Schematics of synthesis of A-Ni-C. b) Cyclic voltammograms of HCl-Ni@C at different cycles. c) Oxidation peaks of HCl-Ni@C in different cycles. d) XRD patterns of the Ni@C, HCl-Ni@C, and A-Ni-C. e, f) HR-TEM images of HCl-Ni@C (e) and A-Ni-C (f). The inset in (f) is the corresponding size distribution of Ni species. a–f) Reproduced under the terms of the CC-BY Creative Commons Attribution 4.0 International license (<https://creativecommons.org/licenses/by/4.0/>).^[72] Copyright 2016, The Authors, published by Springer Nature.

forms of the target material would be oxidized and leached out (Figure 5a).^[73] By virtue of a simple model similar to that for computational hydrogen electrode and experimental standard reduction potentials, the authors predicted the threshold potential, U_n , for leaching one metallic atom from the relevant particular M_n /substrate, in accordance with the experiments. Pt loaded on N-doped porous graphene (NC) as an example was first investigated (Figure 5a). Considering that N-doping usually induces single and double vacancies (SV and DVs) in graphene, a 6×6 supercell of graphene with two DVs and one SV was modelled for NC to load Pt₂₀ nanoparticles, wherein two Pt atoms at DVs and Pt₁₈ NP at SV (Figure 5b). Subsequently, the corresponding U_n values to leach every Pt atom from $n = 20$ to 1 were calculated. As shown in Figure 5b, all 18 Pt atoms at SV were leached out to form Pt²⁺ in aqueous electrolyte at the potential of 0.67 V, leaving two Pt SAs at the DV defects which were coordinated by four N atoms. Higher potential of $U > 1.80$ V would further leach the two Pt SAs out. This means a wide potential window of 1.13 V, within which all the Pt nanoparticles except for the strongly bound SA are electrochemically leached away from the NC surface into the electrolyte, such that high-purity Pt₁/NC with high-loading can be obtained without precise controlling. Similarly, this strategy can be extendable to electrochemically etch Pd₂₀/NC and Ni₂₀/NC (Figure 5b) with the potential windows of 0.55–1.53 V and –0.33 to 0.91 V, respectively. Besides NC, another typical substrate of Fe₂O₃ was also examined by the authors to support the SAs of Pt (Figure 5c,d), Pd, and Ni. Following the modeling for the NC case, a Pt₂₀ nanoparticle was initially deposited on

the O-terminated α -Fe₂O₃(0001) surface with the spontaneous bonding of interlayer Pt₂₀ and surface oxygen (Figure 5d). As shown in Figure 5c, the 17 Pt atoms in the nanoparticle can be leached out at $U = 0.82$ V, leaving three Pt atoms atomically dispersed on Fe₂O₃ which are coordinated with three or four surface O atoms. Further leaching these well-anchored SAs required the potential higher than 1.05 V. Thus, a large window of U spanning 0.23 V can be used to fabricate Pt₁/Fe₂O₃. Akin to Pt SAs, Pd and Ni SAs anchored on Fe₂O₃ can also be obtained at the windows of U ranging from 0.61 to 0.82 V and 0.01 to 0.37 V, respectively. Note that this EcPW strategy is also powerful to achieve single-cluster catalysts like M₃/graphdiyne (M = Pt, Pd, Ni). Compared with traditional chemical etching that uses cyanide to leach Au, O₂ to remove Pt, and CO to etch Rh, the present method is simpler and more applicable, which avoids the accurate tailoring of specific chemical interactions for any target metals. The authors found that the EcPW arises from the strong locally bonding of SAs with substrates. For instance, on the NC and Fe₂O₃, a 10 SA group was coordinated to four N or O atoms with a square planar configuration (Figure 5b,d), and its $d_{x^2-y^2}$ orbital was largely split to stabilize the binding via the bonding contribution below Fermi level and antibonding interaction above Fermi level, as revealed by the integrated projected crystal orbital Hamilton population (IpCOHP) analysis (Figure 5e). The IpCOHP summed overall ligands of each Pt atom were calculated to be –12.6 and –14.2 eV on NC and Fe₂O₃, respectively. These values are both more negative than that for Pt–Pt bonds in bulk Pt metal (–6.0 eV), indicating the stronger binding of Pt SA with substrates. Electron density difference

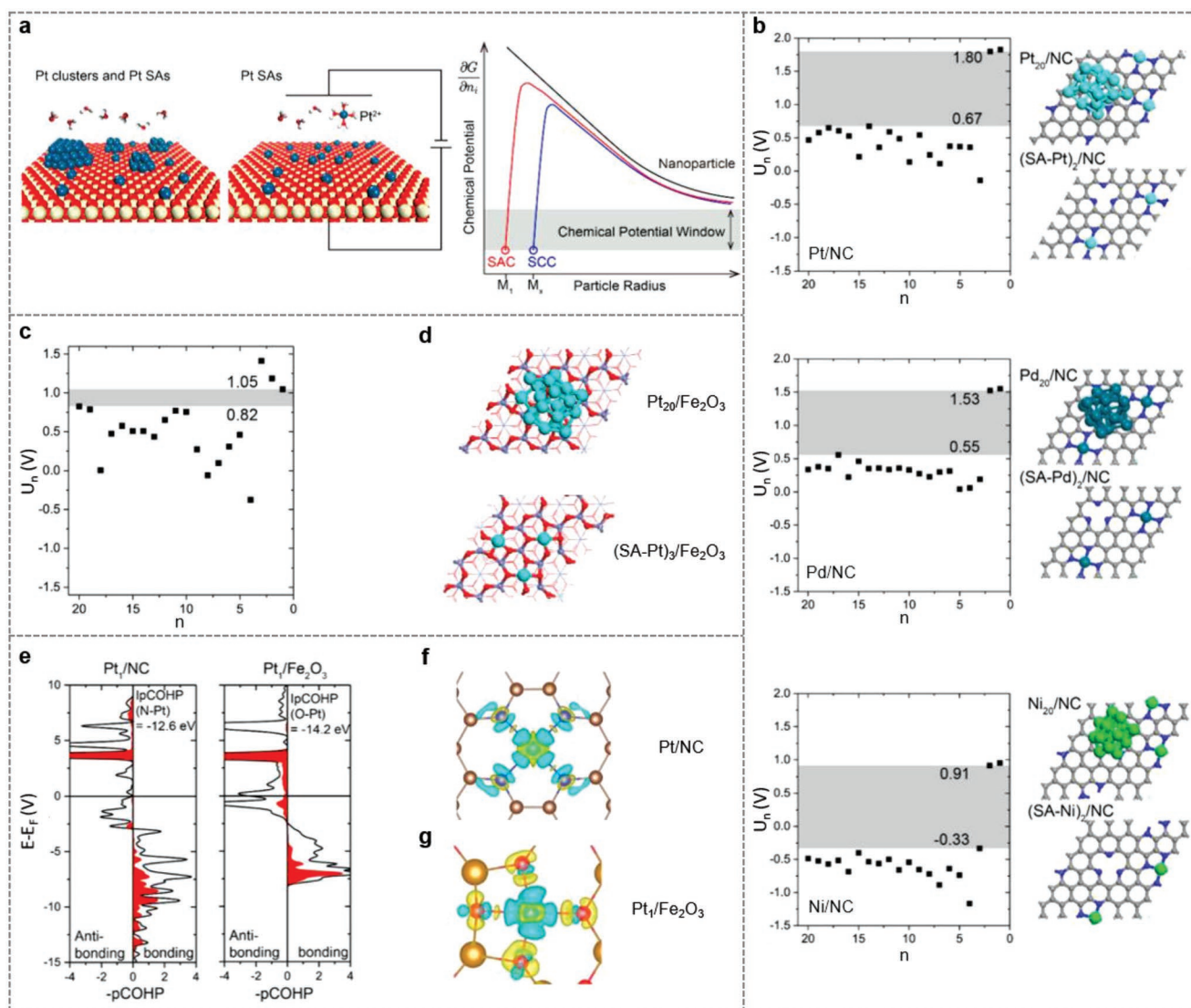


Figure 5. a) Schematics of electrochemical etching to obtain Pt single atoms (SAs) on the substrate (middle) from the aggregate and SA forms (left) within the EcPW, along with the general trends of chemical potentials ($\partial G/\partial n_i$) for three typical cases with respect to particle sizes (right). b) Threshold leaching potentials (U_n vs SHE) for M_n/NC (left), and the optimized configurations of M_{20}/NC and $(SA-M)_2/NC$ (right). c) U_n (vs SHE) and d) the relevant optimized configurations for Pt_n/Fe_2O_3 . e) Projected crystal orbital Hamilton populations (pCOHP) for N–Pt (left) and O–Pt. f, g) Calculated electron density differences of Pt SAs on NC (f) and Fe_2O_3 (g). a–g) Reproduced with permission.^[73] Copyright 2020, American Chemical Society.

analysis (Figure 5f,g) showed that this strong binding leads to apparent electron transfer from Pt SA to adjacent N or O with the Bader charges of Pt atoms to be +1.00 and +1.41|e| on NC and Fe_2O_3 , respectively, different from the neutral charge of Pt atoms in an aggregated form.

3.2. Direct Electrodeposition (DED)

Contrary to the top-down electrochemical etching (ECE), direct electrodeposition (DED) is a bottom-up route which utilizes metal-ion solutions as precursors to access SAs with the assistance of applied currents or potentials. A library of SASCs involving both precious and nonprecious metals have been prepared recently by several research groups.

Bard's group firstly reported the direct atom-by-atom electrodeposition of Pt SAs or small clusters up to 9 atoms on Bi ultramicroelectrodes (UMEs) with radius of 253 nm, followed by electrochemical size estimation via HER (Figure 6a).^[74] Such a precise control was achieved by using ultralow concentrations of the H_2PtCl_6 precursor (150×10^{-15} M) and pulse potentials (switching between 0 and -0.55 V vs Ag/AgCl). Moreover, the UMEs enabled a single nucleus formation rather than multiple deposits. With the sophisticated design, the deposition rate of Pt atom can be slowed down to 0.1 s⁻¹. Size characterization of the deposited Pt_n was realized by investigating their electrocatalytic HER. With the suppression of proton ions bulk migration and diffuse-layer effect, the limiting diffusion current (i_l) for a steady-state HER can be used to determine the radius of electrodeposited Pt species following the formula of $i_l = nF[2\pi]Dcr$,

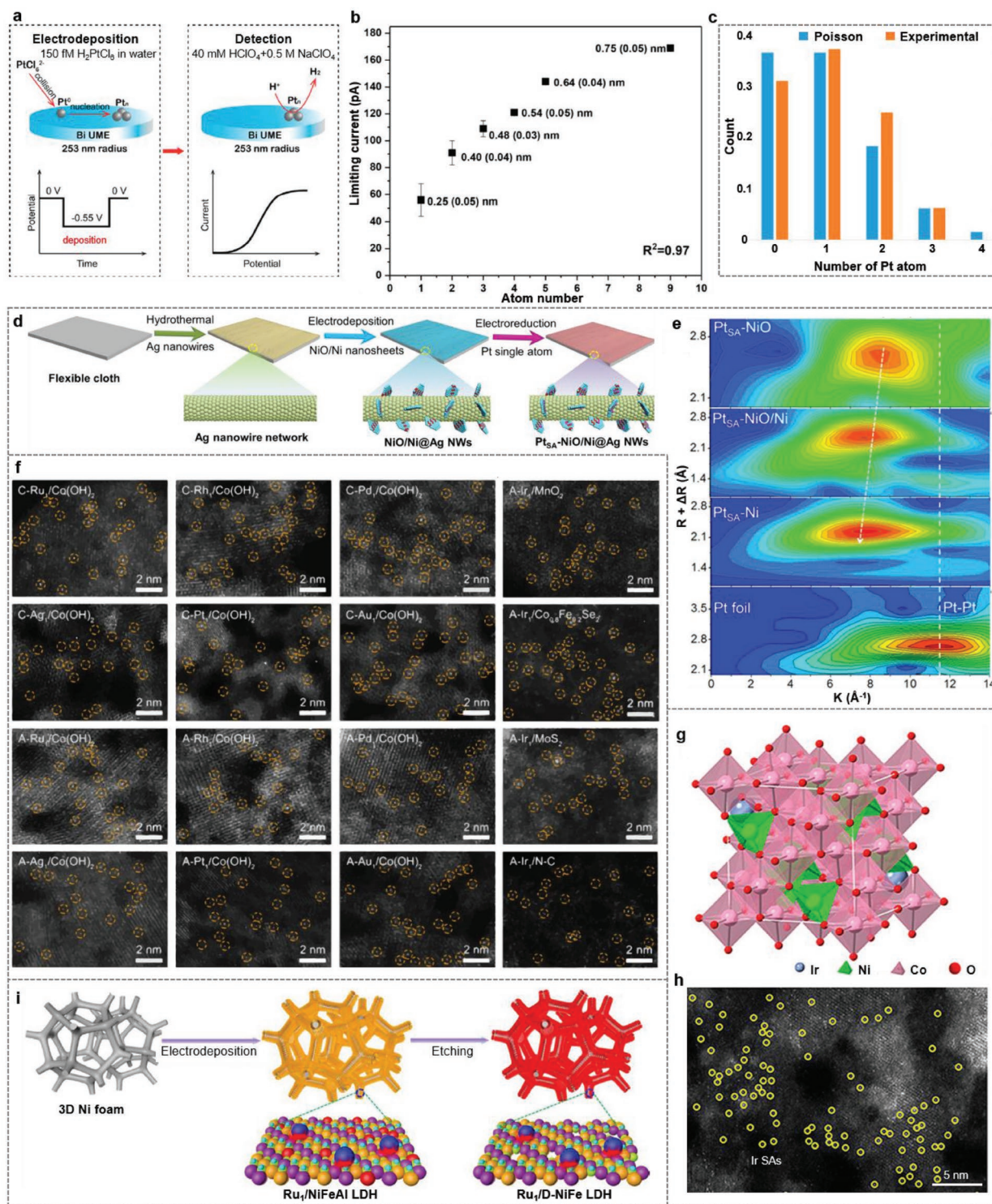


Figure 6. a) Schematics of direct electrodeposition of Pt_n, and subsequent detection by voltammetry of the HER. b) Limiting current-estimated atom number correlation. c) Histogram of the atom number with 10 s deposition calculated by the limiting current overlaid with the Poisson distribution. a–c) Reproduced with permission.^[74] Copyright 2017, American Chemical Society. d) Schematics of the synthesis of Pt_{SA}-NiO/Ni on Ag nanowires network. e) EXAFS wavelet-transform plots of Pt_{SA}-NiO/Ni, Pt_{SA}-NiO, Pt_{SA}-Ni, and Pt foil. d,e) Reproduced under the terms of the CC-BY Creative Commons Attribution 4.0 International license (<https://creativecommons.org/licenses/by/4.0>).^[76] Copyright 2021, The Authors, published by Springer Nature. f) HAADF-STEM images of various single atoms on different substrates by cathodic and anodic electrodeposition. Reproduced under the terms of the CC-BY Creative Commons Attribution 4.0 International license (<https://creativecommons.org/licenses/by/4.0>).^[78] Copyright 2020, The Authors, published by Springer Nature. g) Structure and h) HAADF-STEM image of Ir-NiCo₂O₄. g,h) Reproduced with permission.^[80] Copyright 2020, American Chemical Society. i) Schematics of one-step electrodeposition of Ru₁/NiFeAl LDH. Reproduced under the terms of the CC-BY Creative Commons Attribution 4.0 International license (<https://creativecommons.org/licenses/by/4.0>).^[81] Copyright 2021, The Authors, published by Springer Nature.

in which r is the radius of Pt_n , $D = 1.2 \times 10^{-5} \text{ cm}^2 \text{ s}^{-1}$ is the diffusion coefficient of H_2PtCl_6 , and $c = 150 \times 10^{-15} \text{ M}$ is the concentration of H_2PtCl_6 . For example, the measured smallest i_1 gave a r value of $0.25 \pm 0.05 \text{ nm}$ which is very close to the reported result of Pt atom. Assuming the close-packed arrangement of Pt atoms on Bi UMEs, the number of atoms in a cluster can be calculated through dividing the area of the cluster by that of a single atom. Accordingly, the empirical values for number of Pt atoms in Pt_n can be obtained from the limiting current (Figure 6b). Repeated experimental trials of 16 times with a deposition time of 10 s were conducted and the distribution of numbers of Pt atoms was in line with the computed Poisson distribution (Figure 6c), indicative of a stochastic nature of Pt atom deposition process. Later, the same group found that Pb UMEs are also suitable for controlled electrodeposition of Pt SAs, plus clusters.^[75]

Besides the metallic substrates, Wang and co-workers reported that the 3D Ag nanowires (NWs)-supported 2D NiO/Ni heterostructure can be employed to load Pt SAs.^[76] As shown in Figure 6d, the Ag NWs were first grown on flexible carbon cloth hydrothermally followed by a facile constant-potential electrodeposition of Ni/NiO composite. The crystal-lattice dislocation and phase transition in NiO/Ni heterostructure induced abundant voids and O vacancies, providing efficient sites to trap Pt SAs. As a result, the Pt SAs-immobilized NiO/Ni ($\text{Pt}_{\text{SA}}\text{-NiO/Ni}$) can be obtained by sequential electrodeposition (reduction) with cyclic voltammetry (CV) at a scan rate of 50 mV s^{-1} between 0 and -0.50 V versus RHE for 200 cycles, in 1.0 M KOH solution containing $50 \times 10^{-6} \text{ M}$ H_2PtCl_6 . To precisely clarify the atomic coordination of Pt in $\text{Pt}_{\text{SA}}\text{-NiO/Ni}$, the wavelet transform analysis was carried out due to its high-resolution ability in K spaces and radial distance, such that the atoms with similar configurations can be discriminated. As demonstrated in Figure 6e, the intensity maximum at 11.5 \AA^{-1} corresponding to Pt–Pt coordination was invisible for

$\text{Pt}_{\text{SA}}\text{-Ni}$, $\text{Pt}_{\text{SA}}\text{-NiO}$, and $\text{Pt}_{\text{SA}}\text{-NiO/Ni}$, implying the successful loading of Pt SAs in the three supports. In particular, $\text{Pt}_{\text{SA}}\text{-NiO/Ni}$ showed a different intensity maximum with $\text{Pt}_{\text{SA}}\text{-NiO}$ and $\text{Pt}_{\text{SA}}\text{-Ni}$, the value of which (7.6 \AA^{-1}) is smaller than that of $\text{Pt}_{\text{SA}}\text{-NiO}$ (8.5 \AA^{-1}) and larger than that of $\text{Pt}_{\text{SA}}\text{-Ni}$ (7.4 \AA^{-1}), suggestive of the interfacial coordination of Pt atoms in NiO/Ni.

Apart from Pt, the DED has been proved to be powerful to obtain other precious metals-based SAs anchored on various supports. Zhang and co-workers used $0.3 \times 10^{-3} \text{ M}$ HAuCl_4 as the precursor to prepare single-atom Au on NiFe layered double hydroxide (LDH) ($^{\text{s}}\text{Au/NiFe LDH}$) by stepping the potential from an initial value of -0.2 V versus saturated calomel electrode (SCE) to -0.6 V versus SCE for 5 s and then stepping back to initial potential for 5 s for 5 cycles.^[77] HAADF-STEM image suggested the uniformly distributed Au SAs over the NiFe LDH nanosheet. The emergence of the sharp white line peak in the Au L_3 -edge X-ray absorption near edge structure (XANES) spectra of $^{\text{s}}\text{Au/NiFe LDH}$ compared to that of Au foil with almost no white line suggested partially occupied 5d states of Au in $^{\text{s}}\text{Au/NiFe LDH}$. Simulating the Au L_3 -edge XANES spectra revealed an optimal Au–O bond distance of 1.88 \AA , in consistent with experimental results.

Recently, Zeng and Zhou's group demonstrated a universal electrodeposition approach to fabricate a wide range of

noble-metal single atoms (e.g., Ir, Ru, Rh, Pd, Ag, Pt, and Au) on supports including metal (hydr)oxides like $\text{Co}(\text{OH})_2$ and MnO_2 , sulfide (MoS_2), selenide ($\text{Co}_{0.8}\text{Fe}_{0.2}\text{Se}_2$), and N-doped carbon (Figure 6f).^[78] By simply tuning the parameters of linear sweep voltammetry (LSV) like potential windows and sweep times, various SASCs can be obtained by either cathodic (from 0.10 to -0.40 V vs Ag/AgCl) or anodic (from 1.10 to 1.80 V vs Ag/AgCl) deposition in 1.0 M KOH containing $100 \times 10^{-6} \text{ M}$ metal precursors. To demonstrate the synthetic procedure, the authors used the direct electrodeposition (DED) of Ir SAs from $\text{IrCl}_4 \cdot x\text{H}_2\text{O}$ precursor on $\text{Co}(\text{OH})_2$ nanosheets ($\text{Ir}_1/\text{Co}(\text{OH})_2$) as an example. The extended X-ray absorption fine structure (EXAFS) analysis of both cathodically and anodically deposited SASCs ($\text{C-Ir}_1/\text{Co}(\text{OH})_2$ and $\text{A-Ir}_1/\text{Co}(\text{OH})_2$) illustrated the absence of peaks for Ir–Ir coordination, confirming the atomically dispersion of Ir in both samples. Mechanism analysis implied that IrCl_3^+ and $\text{Ir}(\text{OH})_6^{2-}$ are the depositing species for cathodic and anodic deposition, respectively. Notably, HAADF-STEM images revealed that other metal species can be successfully deposited and atomically dispersed on diverse supports under similar synthetic conditions (Figure 6f).

For effectively trapping SAs to alleviate their possible aggregation, the interactions between single metal atoms and supports which play critical roles in regulating the microenvironment of active sites and thus catalytic activity/stability, cannot be negligible. Cao and collaborators established a fundamental understanding of the interactions between supported Ir SAs and two substrates of nickel–iron sulfide (NFS) and hydroxide (NFH).^[79] Typically, the NFS and NFH were prepared on Ni foam by electrodeposition in the electrolyte containing $3 \times 10^{-3} \text{ M}$ $\text{Ni}(\text{NO}_3)_2$ and $3 \times 10^{-3} \text{ M}$ $\text{Fe}(\text{NO}_3)_3$ with and without thiourea as the S source, respectively. After that, noble metal precursors ($50 \times 10^{-6} \text{ M}$ IrCl_3) were added to the electrolyte and CV scanning was conducted between 0.3 to -0.3 V versus Hg/HgO for 15 cycles to get Ir_1/NFS and Ir_1/NFH . Both the Ir_1/NFS and Ir_1/NFH exhibited similar morphology and Ir loading. However, HAADF-STEM images unveiled a higher surface density of Ir SAs on NFS compared with NFH substrate, presaging the different interactions between Ir SAs and the two substrates. Further investigation of the valence states of Ir confirmed that the chemical interaction in Ir_1/NFS is weaker than in Ir_1/NFH as the binding energy of Ir_1/NFS (62.9 eV for Ir $4f_{7/2}$) is lower than that of Ir_1/NFH (63.2 eV for Ir $4f_{7/2}$). This weaker interaction between the Ir atom and NFS substrate is beneficial for catalytic OER which will be discussed in more detail in the next section. It is worthy to note that such electrodeposition method can be extended to synthesize other M_1/NFS and M_1/NFH ($\text{M} = \text{Pt, Au, Ru}$).

It can be seen that the preloading of various supports is necessary to anchor SAs in these strategies mentioned above. To simplify the synthetic procedures, one-step co-electrodeposition has been explored. For example, Xi and co-workers successfully obtained the Ir SAs on NiCo LDH by constant potential electrolysis (-1.0 V vs Ag/AgCl for 15 min) in the electrolyte containing $\text{Ni}(\text{NO}_3)_2$, $\text{Co}(\text{NO}_3)_2$, and $\approx 45 \times 10^{-6} \text{ M}$ H_2IrCl_6 .^[80] Even annealing in air at $300 \text{ }^\circ\text{C}$, the atomic dispersion of Ir can be still maintained (Figure 6g,h), while the NiCo LDH was converted to NiCo_2O_4 . Structural analysis by XAS and electron spin resonance (ESR) indicated that the atomic Ir anchors

on the lower coordinated Co sites nearby the oxygen vacancies (Figure 6g), promoting the surface electronic exchange-and-transfer capabilities. Hou's group described an analogous constant potential coelectrodeposition of Ru₁/NiFeAl LDH in the corresponding precursor solution containing Ni(NO₃)₂, Fe(NO₃)₃, Al(NO₃)₃, and RuCl₃ (Figure 6i).^[81] To introduce defects, additional chemical etching by NaOH was conducted to remove Al species, and the defect-enriched NiFe LDH anchored Ru SAs (Ru₁/D-NiFe LDH) can be yielded. The obtained SASCs exhibited strong electronic coupling between Ru SAs and the defective NiFe LDH nanosheets evidenced by the positive shift of 0.5 and 0.3 eV in the Ni and Fe XPS spectra compared to bare NiFe LDH, respectively. This metal–support interaction was achieved by the Ru–O coordination with a coordination number of 3.7 obtained by fitting the Fourier transform (FT)-EXAFS spectra.

Additionally, SASCs based on nonprecious metals can be acquired by the direct electrodeposition (DED) as well. Li's group used the constant current electrolysis (chronopotentiometry) at 10 mA cm⁻² to prepare Ni- and Fe-SAs anchored on graphdiyne (Ni/GD and Fe/GD), as schematically depicted in Figure 7a.^[82] The sp hybridization of –C≡C– in GD allowed arbitrary angle rotation of π/π^* perpendicular to the axis, rendering it the ability of chelating a single metal atom without any pretreatment. Both individual Ni and Fe atoms (white dots) can be clearly evidenced in the corresponding HAADF-STEM images of Ni/GD and Fe/GD (Figure 7b,c), excluding the formation of any aggregates. Also, ex situ EXAFS spectra of both Ni/GD and Fe/GD presented only notable peaks at ≈ 1.6 and ≈ 1.5 Å, attributable to Ni–C and Fe–C coordination, respectively, without the peaks in the region of 2–3 Å for Ni–Ni and Fe–Fe (Figure 7d,e), strongly confirming the only existence of Ni- and Fe-SAs. To further identify the Ni–C and Fe–C binding, combined bond length and adsorption energy analysis unveiled the strong chemisorption character and strong charge transfer from Ni/Fe to GD due to the (sp)-d orbital overlapping (Figure 7f).

Xia's group developed a surface-limited underpotential deposition (UPD) technique to obtain Cu SAs site-specifically deposited onto the chalcogen atoms of transition metal dichalcogenides (TMDs) (Figure 7g).^[83] Different from the traditional electrodeposition of metal nanoparticles that use random conductive supports and classical UPD of 2D metal single layer on a uniform metal support, the proposed site-specific UPD enabled self-termination from further growth beyond the single atom. Specially, the plentiful chalcogen sites with lone-pair electrons on TMD substrates can potentially induce strong coordination and electronic interaction with the deposited metal SAs. In this case, the metal–support interaction is strong enough so that it is energetically more favorable than the metal–metal interaction, thus prohibits subsequent formation of metal–metal bond under UPD potential. To demonstrate the viability of the site-specific UPD of Cu SAs, chemically exfoliated ultrathin MoS₂ nanosheets (ce-MoS₂) were used as prototypical substrate. Figure 7h illustrates the CV curve of 2×10^{-3} M CuSO₄ in Ar-saturated 0.1 M H₂SO₄ solution with ce-MoS₂-loaded GCE as the WE. The CV displayed two notable cathodic peaks (*a* and *b*) at ≈ 0.15 and -0.10 V vs Ag/AgCl attributable to Cu UPD and bulk deposition of Cu, respectively. The two anodic peaks (*b'* and *a'*) corresponded to the oxidative dissolution of bulk Cu and

UPD-formed Cu, respectively. Accordingly, a constant potential of 0.1 V vs Ag/AgCl that is more positive than the equilibrium potential of Cu²⁺/Cu, was applied for 120 s to fabricate Cu-SAs/MoS₂. High-resolution Cu 2p XPS spectra (Figure 7i) of Cu SAs/MoS₂ revealed that the main Cu 2p_{3/2} peak at 932.9 eV is located between Cu⁰ (932.4 eV) and Cu²⁺ (934.7 eV), indicative of the partial-positively charged state due to the electronic interaction between single Cu atom and ce-MoS₂. Along with the decreased binding energy of S 2p, the authors concluded that the Cu adatoms specifically attach to the S atoms. The absence of Cu 2p satellite peaks further confirmed the isolated nature of Cu species in Cu-SAs/MoS₂, which was further substantiated by the formation of diverse metal SAs/MoS₂ via Galvanic replacement of Cu in Cu-SAs/MoS₂, including Sn-SAs/MoS₂ (Figure 7j), Pb-SAs/MoS₂ (Figure 7k), Bi-SAs/MoS₂ (Figure 7l), and so on.

Likewise, single nonprecious metal (hydr)oxides can be also synthesized by direct electrodeposition (DED). Bard's group successfully prepared isolated cobalt oxide molecule (Co₁O_x) and clusters (Co_nO_y) on carbon fiber UME (radius = 80 nm) in 0.1 M phosphate buffer with 900×10^{-15} M Co(NO₃)₂ by constant potential electrolysis (chronoamperometry) at 1.65 V versus RHE for 10–120 s during which Co²⁺ was oxidized to Co³⁺ followed by the formation of Co_nO_y clusters on the initially formed nucleus (Figure 7m).^[84] Then, the voltammograms (Figure 7n) of the deposited materials in 10×10^{-3} M NaOH and 0.2 M NaClO₄ were used to estimate their size on the basis of the linear relationship between limiting current and the equivalent radius (*r_d*) of the deposit (Figure 7o), assuming a model of a hemisphere on an inert planar substrate. The smallest size was calculated to be ≈ 0.2 nm, close to the structural parameter of the reported Co–O distance in the CoO₆ octahedra unit (1.89 Å) as measured by XAS. Zeng's group employed similar substrate, porous carbon (P-C), to anchor Fe₁(OH)_x, which was obtained by anodic electrodeposition (LSV method under a potential window ranging from 1.10 to 1.80 V vs RHE for 5 times) in 1.0 M KOH with 100×10^{-6} M FeCl₃.^[85] As shown in Figure 7p, bright spots were obviously visible in the HAADF-STEM image of Fe₁(OH)_x/P-C, revealing the isolated dispersion of Fe atoms. To elucidate the local environment of Fe atoms in the electrocatalyst, the authors performed EXAFS (Figure 7q) and XANES (Figure 7r) measurements. The EXAFS spectra of Fe₁(OH)_x/P-C showed only a characteristic Fe–O peak at 1.98 Å, without the peaks at 2.47 and 3.33 Å ascribed to Fe–Fe and Fe–O–Fe, respectively, validating the atomic dispersion of Fe species. Further fitting the EXAFS spectra revealed the coordination of a single Fe center with six oxygen atoms in the nearest neighbor, most probably forming a FeO₆ octahedral structure for Fe₁(OH)_x/P-C. Additionally, the C K-edge XANES spectra of Fe₁(OH)_x/P-C showed a weaker peak ascribed to C–C π^* at 285.7 eV and a stronger C–O peak at 288.6 eV relative to that of P-C, suggesting the strong interaction of FeO₆ with P-C via C–O–Fe bonding which was confirmed by their DFT calculations later.

3.3. Electrochemical Leaching–Redeposition (ELR)

The phenomenon of metal dissociation from metals anodes has been previously reported under high potentials in an acidic or

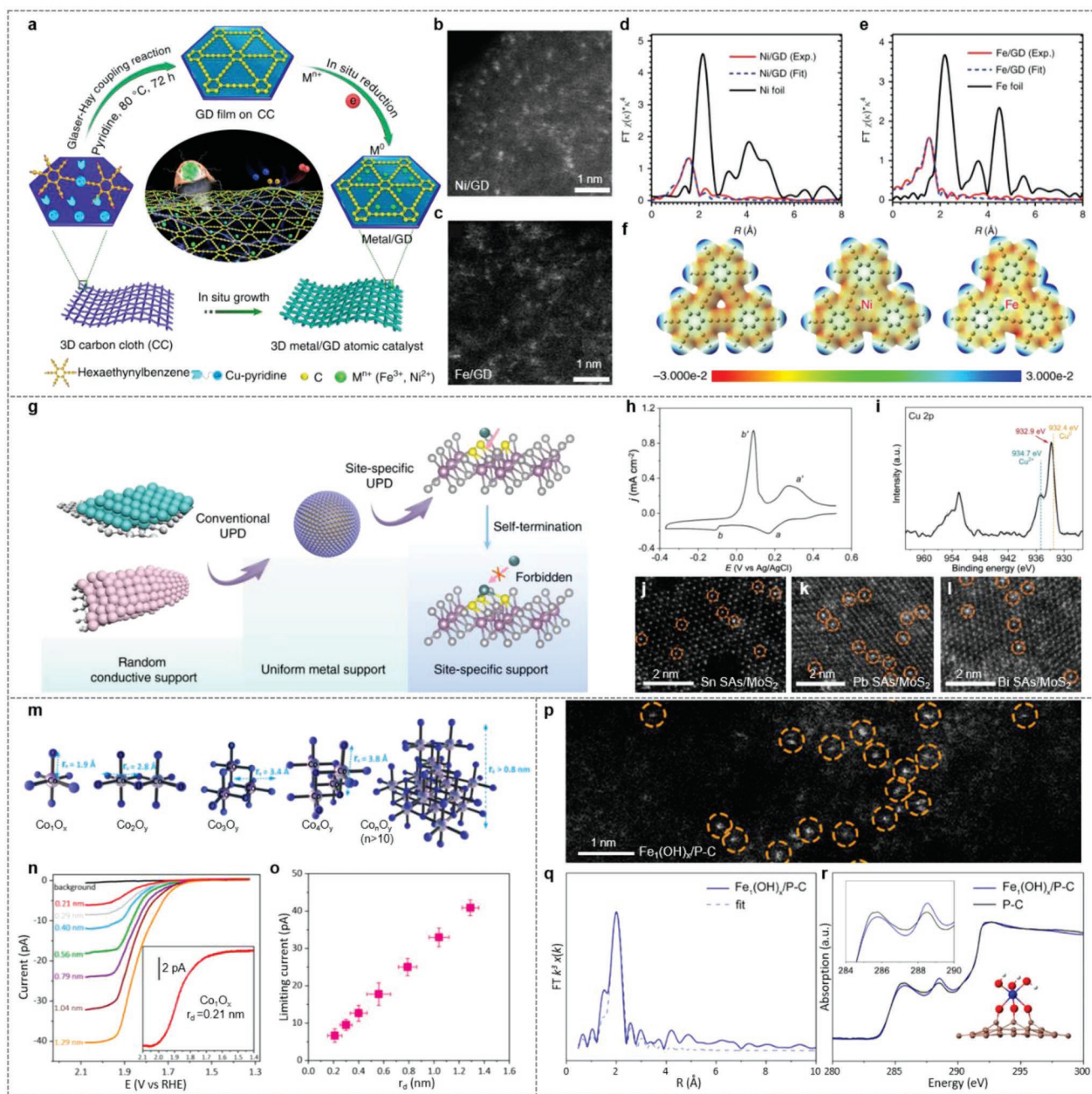


Figure 7. a) Schematics of direct electrodeposition of Ni/GD and Fe/GD. b,c) HAADF-STEM images of Ni/GD (b) and Fe/GD (c). d,e) Ex situ EXAFS spectra of Ni/GD and Ni foil at the Ni K-edge (d) and Fe/GD and Fe foil at the Fe K-edge (e). f) Electrostatic potential maps of GD, Ni/GD, and Fe/GD. a–f) Reproduced under the terms of the CC-BY Creative Commons Attribution 4.0 International license (<https://creativecommons.org/licenses/by/4.0/>).^[82] Copyright 2018, The Authors, published by Springer Nature. g) Comparison of traditional electrodeposition, UPD, and the site-specific electrodeposition on transition metal dichalcogenides. h) CV curve of ce-MoS₂-loaded GCE in Ar-saturated 0.1 M H₂SO₄ + 2 × 10⁻³ M CuSO₄ at 20 mV s⁻¹. i) Cu 2p XPS spectra of the Cu-SAs/MoS₂. j–l) HAADF-STEM images of Sn-SAs/MoS₂ (j), Pb-SAs/MoS₂ (k), and Bi-SAs/MoS₂ (l) by galvanic displacement of Cu-SAs/MoS₂. g–l) Reproduced under the terms of the CC-BY Creative Commons Attribution 4.0 International license (<https://creativecommons.org/licenses/by/4.0/>).^[83] Copyright 2020, The Authors, published by Springer Nature. m) Schematic of Co₁O_x and Co_nO_y. n) Voltammograms of Co₁O_x and Co_nO_y in 10 × 10⁻³ M NaOH + 0.2 M NaClO₄ at 10 mV s⁻¹. o) Limiting currents of SAs or clusters as a function of the estimated equivalent radii. m–o) Reproduced with permission.^[84] Copyright 2020, The Authors, published by National Academy of Sciences, USA. p) HAADF-STEM image of Fe₁(OH)_x/P-C. q) EXAFS spectra at Fe K-edge and the fitting for Fe₁(OH)_x/P-C. r) C K-edge XANES spectra of Fe₁(OH)_x/P-C and P-C. The blue, red, brown, and white spheres represent Fe, O, C, and H atoms, respectively. p–r) Reproduced with permission.^[85] Copyright 2021, American Chemical Society.

alkaline electrolyte, which motivated a new route for the generation of SASCs called electrochemical leaching–redeposition

(ELR). This method contains initial electrochemical leaching of metals from metallic anodes (e.g., Pt anode) and sequential

deposition onto the opposite cathodes to obtain single-atom metals. For example, the onset potential of Pt dissolution is 1.1 V vs RHE in sulfuric acid and with potentials exceeding this value, the soluble platinum species can be obtained from anodic dissolution of Pt electrode, which can then be electrodeposited on the cathodic working electrode (WE). Laasonen and co-workers successfully deposited pseudo-atomic-scale Pt on SWNT-coated GCE (SWNT/at-Pt) with mass loading of 0.06 and 0.3 wt% via potential cycling between -0.55 and 0.25 V vs RHE in 0.5 M H_2SO_4 for 200 or 400 cycles, respectively.^[86] Although the mass loading of Pt for the sample obtained at 400 cycles is ultralow, there still exists several Pt rafts and Pt clusters. Following this, Luo and co-workers for the first time reported the synthesis of Pt SAs anchored on CoP-based nanotube arrays

(NT) with Ni foam (NF) as support (PtSA-NT-NF) in a neutral media (Figure 8a).^[87] With the NF supported CoP-based NT (NT-NF, Figure 8b), a saturated calomel electrode (SCE), and a Pt foil as the WE, reference electrode (RE), and CE, respectively, the potential cycling was conducted between -0.83 and 0 V versus RHE under a scan rate of 150 mV s^{-1} in neutral PBS solution. Different numbers of potential cycling ranging from 2500 to 10 000 were performed and the corresponding LSVs were measured as well. The changing catalytic performance toward HER for the samples obtained with 0, 2500, and 5000 cycles indicated a structural change of the NT-NF, and the overlapping LSV curves for samples with cycle number larger than 5000 suggested a stable structure of the formed electrocatalyst. The PtSA-NT-NF obtained with 5000 cycles was then

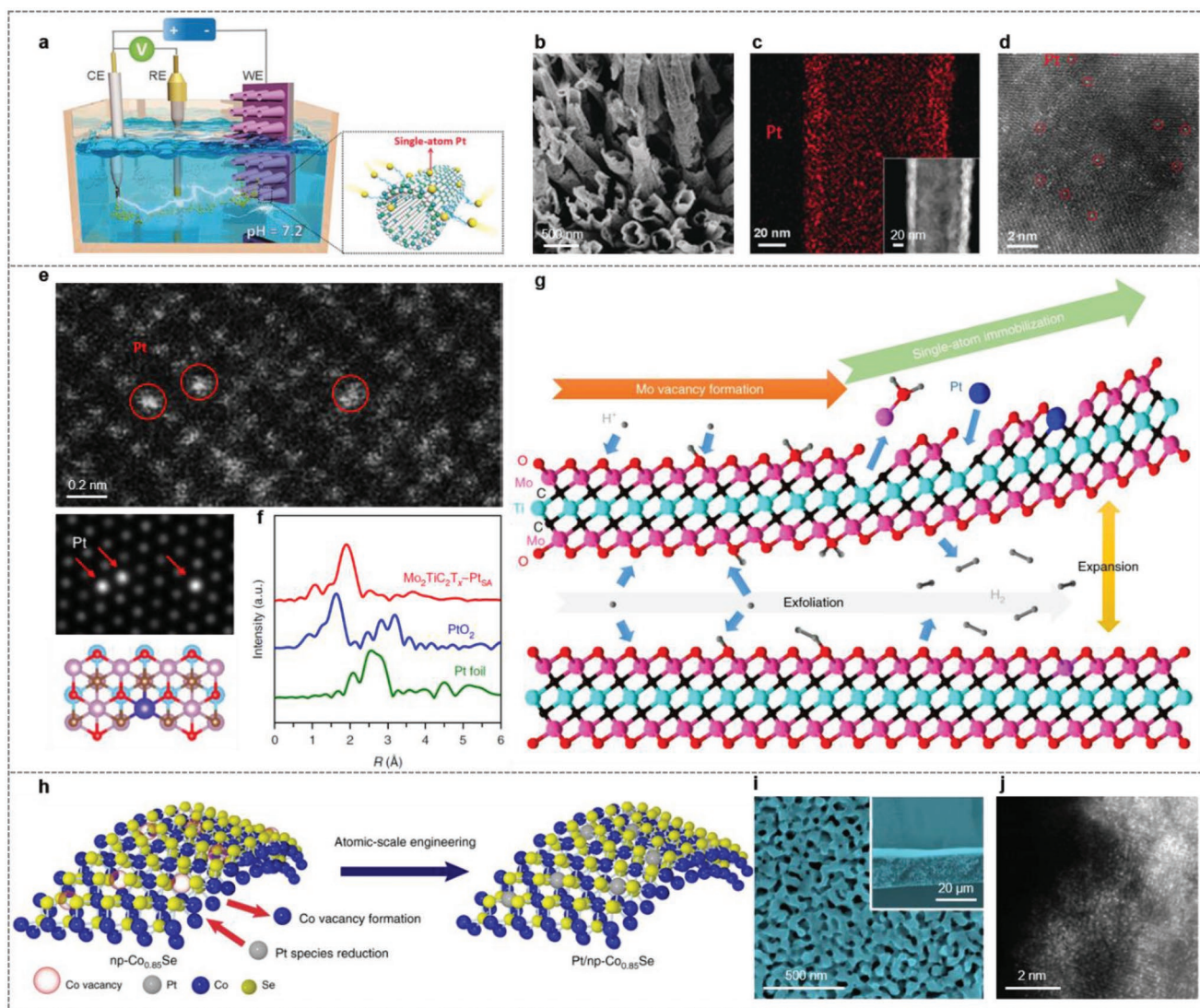


Figure 8. a) Schematics of electrochemical leaching–redeposition of PtSA-NT-NF. b) SEM, c) elemental mapping, and d) HAADF-STEM images of PtSA-NT-NF. a–d) Reproduced with permission.^[87] Copyright 2017, The Authors, published by Wiley-VCH. e) HAADF-STEM image along with the relevant simulated image and the structure illustration of $\text{Mo}_2\text{TiC}_2\text{T}_x\text{-Pt}_{\text{SA}}$. f) EXAFS spectra of Pt foil, PtO_2 and $\text{Mo}_2\text{TiC}_2\text{T}_x\text{-Pt}_{\text{SA}}$. g) Illustration of the synthesis mechanism for $\text{Mo}_2\text{TiC}_2\text{T}_x\text{-Pt}_{\text{SA}}$ during the HER process. e–g) Reproduced with permission.^[88] Copyright 2018, The Authors, published by Springer Nature. h) Schematic of the fabrication of $\text{Pt}/\text{np-Co}_{0.85}\text{Se}$. i) SEM and j) HAADF-STEM images of $\text{Pt}/\text{np-Co}_{0.85}\text{Se}$. Inset in (i) is the cross-sectional image. h–j) Reproduced under the terms of the CC-BY Creative Commons Attribution 4.0 International license (<https://creativecommons.org/licenses/by/4.0>).^[91] Copyright 2019, The Authors, published by Springer Nature.

used as model electrocatalyst. Elemental mapping imaging confirmed the redeposition of Pt on NT-NF (Figure 8c). Furthermore, HAADF-STEM imaging indicated well-dispersed single Pt atoms without granular Pt crystals (Figure 8d). This was further confirmed by the absence of diffraction spots of crystalline Pt in the electron diffraction pattern as well as the missing signal of crystal Pt in the XRD pattern.

Wang and co-workers further refined the ELR of Pt by substituting the NT-NF supports with a double transition metal MXene nanosheets ($\text{Mo}_2\text{TiC}_2\text{T}_x$) on carbon cloth (CC) as the WE.^[88] The electrochemical leaching–redeposition (ELR) was also conducted using a three-electrode system but with repeated LSV scans from 0 to -0.6 V versus RHE in 0.5 M H_2SO_4 . HAADF-STEM imaging of the resulting $\text{Mo}_2\text{TiC}_2\text{T}_x$ -Pt_{SA} illustrated clear bright spots, suggesting heavy and individual Pt SAs on the MXene nanosheets (Figure 8e, upper). Notably, the Pt atoms were immobilized exactly at the Mo positions on $\text{Mo}_2\text{TiC}_2\text{T}_x$, which was further confirmed by STEM simulation and DFT-based structural optimization (Figure 8e, lower). XPS spectroscopy revealed the blueshifted binding energies for Pt 4f (75.6 and 72.0 eV) compared to that of commercial Pt/C catalyst (74.8 and 71.5 eV), indicating that the Pt atoms are mainly in its oxidized states. This was further demonstrated by the XANES spectra at the Pt L₃-edge in which the white line area is proportional to the 5d-electron vacancies.^[89] The results showed that the white line peak intensity of the $\text{Mo}_2\text{TiC}_2\text{T}_x$ -Pt_{SA} lies in between those of PtO₂ and Pt foil, indicative of oxidation state of Pt SAs. Fitting the EXAFS spectra gave a coordination number of 3 for Pt assignable to Pt–C bonds. Additionally, the $\text{Mo}_2\text{TiC}_2\text{T}_x$ -Pt_{SA} showed a peak distinct from that of Pt foil with the absence of Pt–Pt contribution located at ≈ 2.7 Å, indicative of the atomic dispersion of Pt in the $\text{Mo}_2\text{TiC}_2\text{T}_x$ -Pt_{SA}. The XPS and XAS results together provided cogent evidence for the formation of Pt SAs and its strong interaction with the MXene support, which would efficiently prevent the aggregation of Pt SAs. Based on these analyses, the authors proposed a mechanism for the electrochemical process (Figure 8g) during which the $\text{Mo}_2\text{TiC}_2\text{T}_x$ was exfoliated into nanosheets by the formation of H₂ bubbles on the interlayer space following the Heyrovsky process. More importantly, Mo vacancies were generated at the same time by the breaking of C–Mo bonds induced by the strong Mo–O bond in Mo–OH₂, providing sufficient surface vacancies that can effectively serve as the anchoring sites for Pt SAs. The dissolved Pt from the Pt foil counter electrode (CE) were then trapped by the Mo vacancies, forming covalent bonds between the Pt atom and the surrounding C atoms from the MXene framework.

Chronoamperometry has also been applied for the preparation of Pt SAs anchored on other 2D supports like 1T- or 2H-MoS₂.^[90] In this study, Sun and co-workers systematically investigated the effect of anode (Pt foil as WE) potential and deposition time on the dispersion of Pt. It is widely accepted that the higher anode potential, the higher concentration of dissolved Pt and thereby, higher deposition rate. However, with anode voltage higher than 2.3 V vs RHE, the authors found that Pt NPs rather than Pt SAs formed on the 2H-MoS₂. With an anode potential of 2 V, deposition of single-atom Pt was achieved in the first 4–6 h with a nearly constant deposition rate. Beyond 12 h, the formation of Pt NPs was spotted.

HAADF-STEM and elemental mapping revealed the homogeneous distribution of Pt SAs on the Mo vacancies and S vacancies of 2H-MoS₂ support with a Pt content of about 1.1 at%. Based on the intensity analysis of HAADF-STEM images, Pt SAs were primarily immobilized on the Mo vacancy sites rather than the S vacancies. The electrodeposition of other metal SAs (Au and Pd) has also been demonstrated using different anode potentials (1.8 and 1.6 V vs RHE).

Inspired by electrochemical leaching–redeposition (ELR) of Pt SAs based on the potential cycling and Mo vacancy manufacture, Tan's group constructed a single-atom Pt decorated nanoporous cobalt selenides (Pt/np-Co_{0.85}Se, Figure 8h–j).^[91] Nanoporous cobalt selenide (np-Co_{0.85}Se) was used as the WE in this case to generate Co vacancies during the potential cycling (Figure 8i), which can then act as immobilization sites for Pt SAs dissolved from Pt foil CE. A similar phenomenon of Pt aggregation was observed when the CV cycles reached 6000. XPS spectra showed that two peaks associated with Pt 4f orbitals are at 71.8 eV and 75.1 eV for Pt/np-Co_{0.85}Se, higher than that of Pt/C control (71.2 and 74.5 eV), confirming the higher oxidation states of Pt in Pt/np-Co_{0.85}Se. The Co 2p XPS spectra demonstrated positive energy shift with a higher Co³⁺ to Co²⁺ ratio for Pt/np-Co_{0.85}Se (2.27) than that for np-Co_{0.85}Se (1.02), suggestive of the generation of more Co²⁺ vacancies. Deeper investigation of the electronic states was achieved by XAS with Pt foil, commercial Pt/C and PtO₂ as comparison. The Pt L₃-edge XANES spectra showed a white line intensity of Pt/np-Co_{0.85}Se significantly higher than that of Pt foil and commercial Pt/C, validating the positive valence state of Pt SAs in Pt/np-Co_{0.85}Se. The valence state was determined to be 0.8 by linearly fitting the white line intensity, attributable to the electron transfer from Pt to Se in Pt–Se bonds. In the EXAFS spectra of Pt/np-Co_{0.85}Se, the main peak at 2.03 Å was ascribed to the Pt–Se. The Pt–Pt contribution at 2.68 Å cannot be observed, suggesting the single-atom nature of Pt in the np-Co_{0.85}Se. Also, HAADF-STEM imaging of Pt/np-Co_{0.85}Se illustrated the homogeneous dispersion of individual bright spots assignable to Pt atoms in the lattice of Co_{0.85}Se (Figure 8j), confirming the formation of Pt SAs. In order to slow down the diffusion rate and concentration of metal ions (from CE) around the WE to prevent the nuclei growth and aggregation of Pt atoms, Wu's group added a graphene oxide membrane between the WE and CE to filter the soluble Pt species due to its narrow interlayer space and plenty of interlayers, which enabled only a small number of Pt species goin through the membrane.^[92] So, the diffusion rate of Pt species was efficiently decreased and most Pt ions were blocked, both of which are beneficial to generate Pt SAs.

With extensive research efforts into the field of SASCs, the major focus is still on maximizing the atom efficiency, several other key issues remained to be addressed including the synergetic effect between two SAs at the atomic level. Aiming on this, Yao's and Jia's groups synthesized a new class of atomic Co–Pt pair carbon/N-based catalyst (A-CoPt-NC) utilizing core–shell Co-NC as the support and precursor.^[93] CV was conducted between 0.1 V and 1.1 V vs RHE for 8000 cycles with Pt wire as the CE. Under the applied cyclic potential, the Co nanoparticle cores were successfully removed to leave a carbon-based hollow shell structure of A-CoPt-NC with trace Co (1.72 wt %)

and Pt (0.16 wt%), as confirmed by both ICP-AES and EDS mapping results. Dark-field STEM imaging illustrated direct evidence of Co dissolution with only Co nanocluster of ≈ 1 nm being observed. Moreover, interstice of the graphitic layers was formed during CV scanning due to partial corrosion of amorphous carbon with less stability, serving as trapping sites to Pt and Co SAs. The fine structures of Pt and Co were then investigated by XANES and EXAFS testing. The atomic dispersion of Pt was validated by the missing scattering peak for Pt–Pt coordination at 2.6 Å and the main peak located at 1.8 Å were ascribed to Pt–C and Pt–N coordination. Interestingly, the control sample of A-CoPt-C without N doping showed an obvious Pt–Pt coordination peak similar to that of Pt foil, highlighting the critical role of N doping in trapping Pt SAs. The statistical distribution of two adjacent metal atoms (40 pairs) showed that the metal–metal distance ranges from 0.2 nm to 0.5 nm and lies mostly in the interval of 0.25–0.29 nm, as verified by the noise-filtered HAADF-STEM image.

Besides the synthesis of precious metal SASCs, non-noble-metal-based SASCs have also been prepared via electrochemical leaching–redeposition (ELR). For example, Wu and co-workers replaced Pt-based CE by Fe foil to access Fe SAs anchored on nitrogen-doped carbon (Fe-SAs/N–C) in an H-cell with 0.5 M H_2SO_4 .^[94] A graphene oxide membrane with the interlay spacing of 10.2 Å was used to filter soluble Fe species to reduce their diffusion and growth. The isolated Fe SAs on N-doped carbon support with a mass loading of 0.54 wt% can be clearly identified on the AC-HAADF-STEM image. Selected-area electron diffraction and XRD consistently demonstrated that there is no crystalline Fe in Fe-SAs/N–C sample. The oxidation state of the Fe SAs was determined to be in the range of Fe^0 – Fe^{2+} through the Fe K-edge spectra with Fe foil, FeO, and Fe_2O_3 as controls. This agreed well with the XPS spectra that showed a peak of Fe $2p_{3/2}$ at 711.4 eV which is smaller than that of Fe^{2+} (712.7 eV) and larger than that of Fe^0 (710.7 eV). In the k^3 -weighted EXAFS spectra, a dominant peak at 1.42 Å from the contribution of Fe–N coordination was observed and the fitted result gave a coordination number of 4 (Fe– N_4). The N 1s XPS spectra revealed four N species of pyridinic-N, graphitic-N, pyrrolic-N, and oxidized pyridinic-N in which the first two kinds accounted for majority of N species in Fe-SA/N–C and acted as anchor sites for Fe SAs.

4. Electrocatalytic Green Hydrogen Cycling

With the maximum atom utilization efficiency and unique electronic structures, SASCs have exhibited remarkable improvements on electrocatalytic activity in a variety of electrochemical reactions, such as water splitting,^[95,96] oxygen reduction,^[97,98] CO_2 reduction,^[36–39] nitrogen/nitrate reduction,^[41–46] biomass upgrading,^[47–50] and so on. In this section, we mainly focus on the electrocatalytic applications for green hydrogen cycling including HER, OER, OWS, and ORR. The hydrogen oxidation reaction (HOR) is not included due to the lack of relevant literature. Table 1 summarizes the electrocatalytic activities (overpotential at a specific current density) of SASCs based on ambient electrosynthesis for different reactions under diverse electrolytes.

4.1. Hydrogen Evolution Reaction (HER)

Pt nanoparticles supported on carbon (Pt/C) is the commercial benchmark catalyst for the hydrogen evolution reaction (HER) in acidic solution, as the metallic Pt possesses the optimal adsorption free energy of H^* (ΔG_{H^*}) which is ≈ 0 eV as well as the highest exchange current density.^[99,100] Due to its scarcity in reserve, it is of crucial importance to boost the mass activity and thus reduce its required amount.^[16] To tackle this issue, a variety of Pt SAs on different substrates have been prepared based on ambient electrosynthesis for efficient HER in all pHs.

For example, Wang and co-workers reported the two-step electrodeposition of $\text{Pt}_{\text{SA}}\text{-NiO/Ni}$ on Ag-NWs-loaded flexible carbon cloth for improved HER in alkaline (1.0 M KOH) solution (Figure 9a–c).^[76] Low overpotentials of only 26 and 85 mV were needed for the $\text{Pt}_{\text{SA}}\text{-NiO/Ni}$ to achieve 10 and 100 mA cm^{-2} , respectively, significantly superior to those of $\text{Pt}_{\text{SA}}\text{-NiO}$, $\text{Pt}_{\text{SA}}\text{-Ni}$, NiO/Ni, and commercial Pt/C. To shed light on their improved HER activity, the authors conducted DFT calculations. Differential charge density analysis displayed the charge delocalizing from Pt to the bonded O atom and charge localizing from adjacent Ni atoms to Pt for the $\text{Pt}_{\text{SA}}\text{-NiO/Ni}$, resulting in a locally enhanced electric field around the Pt site which is more intensive than those of $\text{Pt}_{\text{SA}}\text{-NiO}$ and $\text{Pt}_{\text{SA}}\text{-Ni}$. Moreover, the projected density of states (PDOS) results revealed a wider Pt-5d band and higher density near the Fermi level for $\text{Pt}_{\text{SA}}\text{-NiO/Ni}$ than those for $\text{Pt}_{\text{SA}}\text{-NiO}$, and $\text{Pt}_{\text{SA}}\text{-Ni}$, suggesting Pt SAs coupled with NiO/Ni heterostructure possess more free electrons to favor the H adsorption and transfer. Figure 9a demonstrated that the energy barrier of water dissociation over $\text{Pt}_{\text{SA}}\text{-NiO/Ni}$ is only 0.31 eV, much lower than those of $\text{Pt}_{\text{SA}}\text{-NiO}$ (0.47 eV) and $\text{Pt}_{\text{SA}}\text{-Ni}$ (1.42 eV). Also, the most optimal H binding energy of -0.07 eV (near-zero) was needed for $\text{Pt}_{\text{SA}}\text{-NiO/Ni}$ compared to $\text{Pt}_{\text{SA}}\text{-NiO}$ (0.74 eV) and $\text{Pt}_{\text{SA}}\text{-Ni}$ (-0.38 eV), suggesting the rapid recombination of the dissociated proton for H_2 generation. Benefitting from the optimal charge distribution and Pt-5d band, a Pt mass activity of $\text{Pt}_{\text{SA}}\text{-NiO/Ni}$ at an overpotential of 100 mV was calculated to be high to 20.6 A mg^{-1} , 2.4, 2.3, and 41.2 times greater than those of $\text{Pt}_{\text{SA}}\text{-NiO}$ (8.5 A mg^{-1}), $\text{Pt}_{\text{SA}}\text{-Ni}$ (9.0 A mg^{-1}), and commercial Pt/C (0.5 A mg^{-1}), respectively.

CoP-based nanotube arrays supported Pt SAs (PtSA-NT-NF) were also obtained by Luo and co-workers via electrochemical leaching–redeposition (ELR) for neutral HER (1 M PBS).^[87] Along with the increasing CV cycles, the overpotential at 10 mA cm^{-2} (η_{10}) gradually decreased and then reached a stable state (Figure 9d). Finally, a low η_{10} of only 24 mV was obtained for PtSA-NT-NF. Such a high activity can be ascribed to the high Pt mass utilization and the positively modulated electronic structures by substrates (CoP-based nanotube), along with the decent activity of CoP.^[101,102] Note that at larger current densities (>43 mA cm^{-2}), the PtSA-NT-NF exhibited better performance than Pt/C. A Tafel slope of 30 mV dec^{-1} , similar to that of Pt/C (31 mV dec^{-1}), indicated a Pt-like HER kinetics of PtSA-NT-NF through the Volmer–Tafel mechanism.

Similarly, double transition metal MXene nanosheets ($\text{Mo}_2\text{TiC}_2\text{T}_x$)-stabilized Pt SAs through ELR have also been explored for HER.^[88] As shown in Figure 9e, the HER polarization curves for $\text{Mo}_2\text{TiC}_2\text{T}_x\text{-Pt}_{\text{SA}}$ together with Pt/C, bare

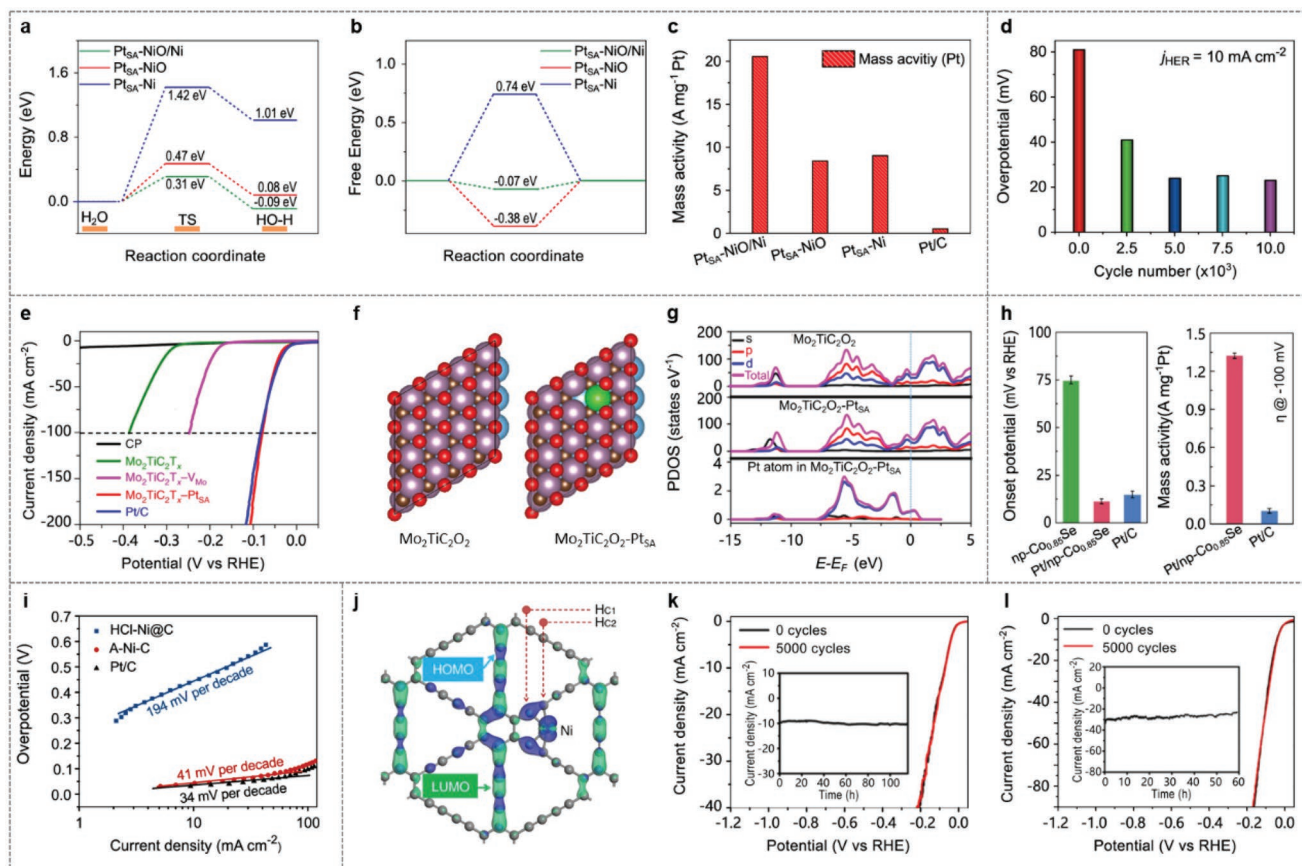


Figure 9. a) Calculated energy barriers of water dissociation kinetic, b) adsorption free energies of H^* , and c) mass activity of Pt_{SA} -NiO/Ni, Pt_{SA} -NiO, Pt_{SA} -Ni, and Pt/C at the overpotential of 100 mV. a–c) Reproduced under the terms of the CC-BY Creative Commons Attribution 4.0 International license (<https://creativecommons.org/licenses/by/4.0/>).^[76] Copyright 2021, The Authors, published by Springer Nature. d) Dependence of the overpotential at 10 $mA\ cm^{-2}$ on the CV cycle number. Reproduced with permission.^[87] Copyright 2017, Wiley-VCH. e) HER polarization curves of carbon paper (CP), $Mo_2TiC_2T_x$, $Mo_2TiC_2T_x-V_{Mo}$, $Mo_2TiC_2T_x-Pt_{SA}$, and Pt/C (40%). f) Slab models of $Mo_2TiC_2O_2$ and $Mo_2TiC_2O_2-Pt_{SA}$. g) Calculated PDOS of $Mo_2TiC_2O_2$ and $Mo_2TiC_2O_2-Pt_{SA}$. e–g) Reproduced with permission.^[88] Copyright 2018, The Authors, published by Springer Nature. h) Onset potential at $-1\ mA\ cm^{-2}$ and mass activity of Pt/ $np-Co_{0.85}Se$ and Pt/C. Reproduced under the terms of the CC-BY Creative Commons Attribution 4.0 International license (<https://creativecommons.org/licenses/by/4.0/>).^[91] Copyright 2019, The Authors, published by Springer Nature. i) Tafel plots of HCl-Ni@C, A-Ni-C and Pt/C. Reproduced under the terms of the CC-BY Creative Commons Attribution 4.0 International license (<https://creativecommons.org/licenses/by/4.0/>).^[72] Copyright 2016, The Authors, published by Springer Nature. j) Real-space HOMO and LUMO contour plots on Ni-on-GD. k, l) Stability tests of Ni/GD (k) and Fe/GD (l). j–l) Reproduced under the terms of the CC-BY Creative Commons Attribution 4.0 International license (<https://creativecommons.org/licenses/by/4.0/>).^[82] Copyright 2018, The Authors, published by Springer Nature.

$Mo_2TiC_2T_x$, and exfoliated $Mo_2TiC_2T_x$ ($Mo_2TiC_2T_x-V_{Mo}$) in 0.5 M H_2SO_4 were collected for comparison. It can be clearly seen that the $Mo_2TiC_2T_x-Pt_{SA}$ exhibited the best HER performance with a η_{10} of 30 mV, much lower than those of control samples and almost identical with that of commercial 40 wt% Pt/C. Specifically, to reach the current densities of 100 and 200 $mA\ cm^{-2}$, the corresponding overpotentials for $Mo_2TiC_2T_x-Pt_{SA}$ were only 77 and 104 mV, respectively. Such superior HER activity of $Mo_2TiC_2T_x-Pt_{SA}$ was further corroborated by its low Tafel slope of 30 $mV\ dec^{-1}$, implying the rapid HER kinetics due to the introduction of Pt SAs. The calculated mass activity of $Mo_2TiC_2T_x-Pt_{SA}$ was 8.3 $A\ mg^{-1}$ at an overpotential of 77 mV, 40 times higher than that of commercial 40 wt% Pt/C (0.21 $A\ mg^{-1}$). These comparisons demonstrated the maximized atomic utilization efficiency in Pt SAs. In addition to excellent electrocatalytic activity, the long-term stability was also gained by atomic dispersion of Pt, with no decay after 100 h stability

test due to the strong electronic interaction between Pt SAs and the exfoliated $Mo_2TiC_2T_x-V_{Mo}$ support. Subsequently, the authors carried out DFT calculations to elucidate the underlying origins of enhanced HER over $Mo_2TiC_2T_x-Pt_{SA}$. On the basis of the systemic physicochemical characterizations (Figure 8e–g), the models of $Mo_2TiC_2O_2$ and $Mo_2TiC_2O_2-Pt_{SA}$ were chosen to represent the structures of $Mo_2TiC_2T_x$ and $Mo_2TiC_2T_x-Pt_{SA}$, respectively, for DFT computations (Figure 9f). It was revealed that the deposition of Pt SAs onto the Mo vacancies effectively delocalizes the charges from Pt to its surroundings and thus leads to a redistribution of the electrons, providing an improved electron environment. Moreover, as depicted by the projected density of states (PDOS) in Figure 9g, the DOS near the Fermi level was elevated after incorporation of Pt atoms due to the contribution from d orbitals of Pt, leading to enhanced conductivity and electrocatalytic activity. In addition, the lower work function of $Mo_2TiC_2O_2-Pt_{SA}$ compared to $Mo_2TiC_2O_2$

indicated the higher electronic energy levels and improved capability of electron-donating. Considering the rate-limiting role of the hydrogen adsorption for acidic HER, the Gibbs free energies of hydrogen adsorption (ΔG_{H^*}) over $\text{Mo}_2\text{TiC}_2\text{O}_2\text{-Pt}_{\text{SA}}$ and $\text{Mo}_2\text{TiC}_2\text{O}_2$ as well as Pt were then calculated. The ΔG_{H^*} on Pt SAs in $\text{Mo}_2\text{TiC}_2\text{O}_2\text{-Pt}_{\text{SA}}$ was low to -0.08 eV, which is close to the optimal value for an ideal HER catalyst ($\Delta G_{H^*} = 0$ eV) and lower than the ΔG_{H^*} of -0.19 eV on Mo–O terminal in the model MXene (MoTiC_2O_2) and -0.10 eV on Pt(111). This weak strength of H^+ adsorption on Pt SAs would facilitate the faster releasing of H_2 . The as-prepared $\text{Mo}_2\text{TiC}_2\text{O}_2\text{-Pt}_{\text{SA}}$ showed excellent HER performance in neutral medium (0.5 M PBS) as well, with an overpotential of only 61 mV at 10 mA cm^{-2} , demonstrating the potential applications in both neutral and acidic electrolytes.

Recently, Tan's group used the HER-active nanoporous $\text{Co}_{0.85}\text{Se}$ to anchor Pt SAs ($\text{Pt/np-Co}_{0.85}\text{Se}$, Figure 9h–j) for neutral HER via the similar ELR method.^[91] As shown in Figure 9h, the onset potential (denoted as the potential to afford -1.0 mA cm^{-2}) of $\text{Pt/np-Co}_{0.85}\text{Se}$ can be reduced to 12 mV from ≈ 75 mV for $\text{np-Co}_{0.85}\text{Se}$, even smaller than that of Pt/C benchmark. Notably, the η_{10} of $\text{Pt/np-Co}_{0.85}\text{Se}$ is only 55 mV, in sharp contrast to that for $\text{np-Co}_{0.85}\text{Se}$ (264 mV). The outstanding HER activity of $\text{Pt/np-Co}_{0.85}\text{Se}$ can also be reflected by the low Tafel slope of 35 mV dec^{-1} relative to Pt/C (37 mV dec^{-1}) and $\text{np-Co}_{0.85}\text{Se}$ (90 mV dec^{-1}), suggesting fast HER kinetics after introducing Pt SAs. The mass activity for HER over $\text{Pt/np-Co}_{0.85}\text{Se}$ at an overpotential of -100 mV was calculated to be 1.32 A mg^{-1} , 11 times greater than that of the commercial 10 wt% Pt/C (0.12 A mg^{-1} , Figure 9h). These results suggested that Pt SAs anchored on $\text{np-Co}_{0.85}\text{Se}$ can maximize the electrocatalytic HER activity and thus decrease the cost of electrocatalysts. Electrochemical impedance spectroscopy (EIS) and electrochemically active surface area (ECSA) analysis uncovered the lower internal resistance and more accessible active sites after Pt SAs incorporation in $\text{np-Co}_{0.85}\text{Se}$, respectively. Besides superior activity, the $\text{Pt/np-Co}_{0.85}\text{Se}$ also showed robust stability, as revealed by the negligible current decay over 40 h in the chronoamperometry curve and undetectable morphology changes. Moreover, the $\text{Pt/np-Co}_{0.85}\text{Se}$ can function well in acidic and basic electrolytes. To gain insights on the improved HER activity of $\text{Pt/np-Co}_{0.85}\text{Se}$, operando XAS measurements and DFT calculations were conducted by the authors. The operando Co K-edge XANES and FT-EXAFS spectra of $\text{Pt/np-Co}_{0.85}\text{Se}$ showed slight shift toward the higher energy, and shrinking of the radial distance of the Co–Se shell with increasing of the operated potential from open circuit voltage (OCV) to -0.2 V vs RHE, respectively, different from $\text{np-Co}_{0.85}\text{Se}$ which showed no distinct changes. These contrasts suggested that the interactions between Pt SAs and $\text{Co}_{0.85}\text{Se}$ facilitate electron transfer from Co to Se atoms during HER, so that the positively charged Co atoms in $\text{Pt/np-Co}_{0.85}\text{Se}$ can easily capture the negative oxygen atom in water molecule to activate it, as confirmed by the enhanced Co–OH shell during HER. The strong interactions between Pt SAs and $\text{Co}_{0.85}\text{Se}$ were substantiated by charge density difference. A strong charge redistribution at Pt-bonding region can be observed in $\text{Pt/np-Co}_{0.85}\text{Se}$, which promoted a significant increase in the internal electron concentration for enhanced HER. The Gibbs free energy of water dissociation ($\Delta G_{\text{H}_2\text{O}}$) over

$\text{Pt/np-Co}_{0.85}\text{Se}$ significantly decreased from 0.891 eV for $\text{np-Co}_{0.85}\text{Se}$ to 0.491 eV which is even lower than that (0.563 eV) of Pt (111), implying an accelerated Volmer process after atomic-level Pt doping. Additionally, the ΔG_{H^*} for $\text{Pt/np-Co}_{0.85}\text{Se}$ at Co sites (-0.083 eV) and at Pt sites (-0.079 eV) were close to the idea value of 0 eV and comparable to that of Pt (111), suggesting the favorable adsorption of H and subsequent combination for H_2 generation.

Zeng's and Hou's groups reported the direct cathodically electrodeposition of diverse metal SAs besides Pt, on various supports like N–C, Co(OH)_2 , and $\text{Co}_{0.8}\text{Fe}_{0.2}\text{Se}_2$ for alkaline HER.^[78] For example, the resulting C– $\text{Ir}_1/\text{N-C}$ and C– $\text{Ir}_1/\text{Co}_{0.8}\text{Fe}_{0.2}\text{Se}_2$ demonstrated higher HER activities compared to commercial Pt/C. In particular, the C– $\text{Ir}_1/\text{Co}_{0.8}\text{Fe}_{0.2}\text{Se}_2$ needed a η_{10} of only 8 mV in 1.0 M KOH.

Apart from electrosynthesis of noble metal-based SAs, HER electrocatalysts based on earth-abundant elements were also obtained as promising alternatives for cost-effective HER. Yao and co-workers reported a nonprecious Ni-based electrocatalyst by etching Ni nanoparticles to leave Ni SAs on graphitized carbon (A–Ni–C).^[72] The as-prepared A–Ni–C electrocatalyst required a η_{10} of only 34 mV in 0.5 M H_2SO_4 , much smaller than that of control HCl–Ni@C sample (440 mV) with higher Ni content. Also, the lower Tafel slope of 41 mV dec^{-1} for A–Ni–C relative to HCl–Ni@C sample (194 mV dec^{-1}) further manifested its exceptional HER kinetics of A–Ni–C (Figure 9i), close to Pt/C (34 mV dec^{-1}). EIS measurements revealed that the charge transfer resistance of A–Ni–C is similar to that of Pt/C, and much lower than that of HCl–Ni@C, indicative of the much faster electron transfer. Chronoamperometry at an overpotential of 45 mV was then applied to assess the stability of A–Ni–C. The current density maintained at 10 mA cm^{-2} during the first 11 h and then gradually increased to 14 mA cm^{-2} due to the activation of the catalyst and finally reached a plateau of 12 mA cm^{-2} with no obvious deactivation during the additional 25 h testings.

Another example of nonprecious SAs-based HER electrocatalysts is the direct electrodeposition of Ni/Fe SAs anchored on GD (Figure 9j–l).^[82] Bond length analysis implied a strong chemisorption and strong charge transfer from Ni/Fe to GD. Using Ni–3d as an example, the authors utilized reported method to ab initio reveal the energy of targeted on-site orbital especially with electronic occupations under different cases of chemical bonding. As shown in Figure 9j, the HOMO and LUMO charge density distributions induced by the stabilized Ni^0 can be seen and the fast ($\text{H}^+ + \text{e}$) charge exchanges were believed to be responsible for the efficient HER. As a result, both the resulting Fe/GD and Ni/GD exhibited satisfactory HER activity in 0.5 M H_2SO_4 with η_{10} of 66 and 88 mV respectively, along with superb stability for 100 h and 5000 cycles (Figure 9k,l). Although these apparent activities were inferior to that of 20 wt% Pt/C benchmark, the Ni/GD and Fe/GD SAECs demonstrated superior mass activity of 16.6 and 80.0 $\text{A mg}_{\text{metal}}^{-1}$, respectively, at the overpotential of 200 mV.

4.2. Oxygen Evolution Reaction (OER)

Compared to the HER with two-electron–proton-transfer process at cathode, the anodic OER comprises complex

four-electron–proton-transfer process with multiple reaction intermediates and suffers from a more sluggish kinetics.^[103–106] It is thus believed that the OER predominantly governs the overall energy conversion efficiency of water splitting.^[107–109] The benchmark OER electrocatalysts in acidic and alkaline solutions are Ir/Ru-based^[110–112] and Ni/Fe/Co-based^[113–115] nano-materials, respectively.^[116,117] While the high cost and limited reserve for noble metals, and mediocre activity of nonprecious metals-based electrocatalysts hinder the large-scale implementation.^[118,119] Therefore, developing SASCs-based OER electrocatalysts with ultimate atom utilization efficiency is imperative to cut down cost and improve energy conversion efficiency.^[120]

Zeng and co-workers reported anodic direct electrodeposition (DED) of a series of noble metal SAs including Ru, Rh, Ag, and Ir, on numerous supports like N–C, Co(OH)₂, MnO₂, Co_{0.8}Fe_{0.2}Se₂, and so on for alkaline OER (1.0 M KOH).^[78] Compared to commercial IrO₂ with a η_{10} of >350 mV, the resulting A-Rh₁/Co(OH)₂, A-Ag₁/Co(OH)₂, A-Ir₁/Co(OH)₂, and A-Ir₁/Co_{0.8}Fe_{0.2}Se₂ all showed decreased overpotentials at the same current density (Figure 10a). Specially, the A-Ir₁/Co_{0.8}Fe_{0.2}Se₂ delivered a η_{10} of only 230 mV, which is 135 mV lower than that

of IrO₂, due to the enhanced charge transfer by strong metal–support interaction and high atomic efficiency. In view of the high HER activity of C-Ir₁/Co_{0.8}Fe_{0.2}Se₂ in the same electrolyte, the authors also assembled the C-Ir₁/Co_{0.8}Fe_{0.2}Se₂ and A-Ir₁/Co_{0.8}Fe_{0.2}Se₂ into a two-electrode cell for overall water splitting.

Likewise, Cao and co-workers directly electrodeposited Ir SAs on nickel–iron-sulfide-loaded Ni foam (Ir₁/NFS) for electrocatalytic OER in 1.0 M KOH.^[79] The η_{10} for Ir₁/NFS was calculated to be only ≈170 mV, much lower than Ir SAs on nickel–iron hydroxide (Ir₁/NFH, ≈190 mV), commercial 5 wt% Ir/C and IrO₂ benchmark (Figure 10b). Remarkably, to deliver 100 and 500 mA cm⁻², the required overpotentials of Ir₁/NFS were 206 and 220 mV, respectively, while the Ir₁/NFH required much higher overpotentials of 234 and 257 mV, respectively. The prominent OER activity of Ir₁/NFS was also corroborated by the small Tafel slope (33 mV dec⁻¹), lower than those of Ir₁/NFH (35 mV dec⁻¹), Ir/C (87 mV dec⁻¹), and IrO₂ (95 mV dec⁻¹). Additionally, the calculated mass activity for Ir₁/NFS based on Ir loading was 20.3 A g⁻¹ at 1.45 V versus RHE, ≈1.55 times higher than that of Ir₁/NFH (13.1 A g⁻¹). The Ir₁/NFS also displayed exceptional long-term electrochemical stability at a

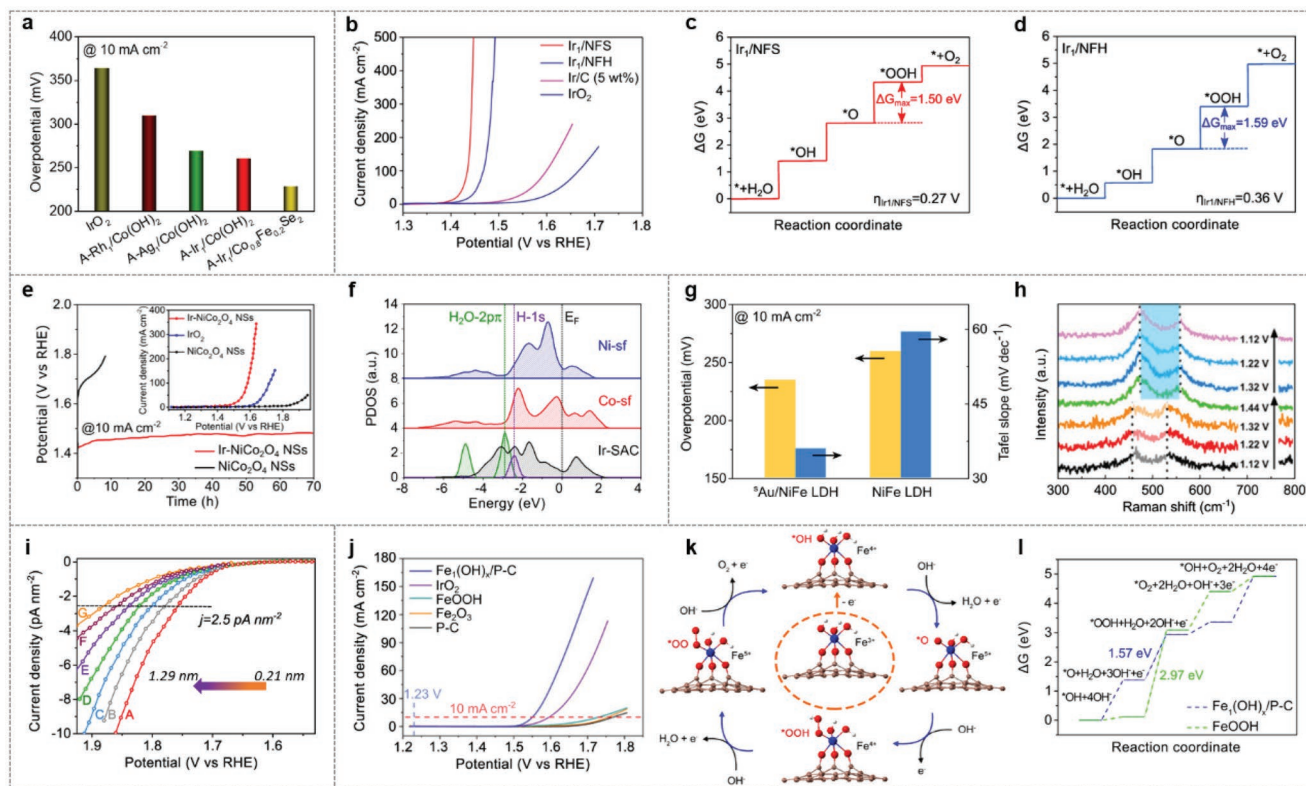


Figure 10. a) Overpotentials at 10 mA cm⁻² for OER in 1.0 M KOH over various SAs-based electrocatalysts. Reproduced under the terms of the CC-BY Creative Commons Attribution 4.0 International license (https://creativecommons.org/licenses/by/4.0).^[78] Copyright 2020, The Authors, published by Springer Nature. b) OER polarization curves of Ir₁/NFS, Ir₁/NFH and control samples in 1.0 M KOH. c, d) Free energy diagram of OER pathway over Ir₁/NFS (c) and Ir₁/NFH (d). b–d) Reproduced under the terms of the CC-BY Creative Commons Attribution 4.0 International license (https://creativecommons.org/licenses/by/4.0).^[79] Copyright 2020, The Authors, published by Springer Nature. e) Chronoamperometric response of NiCo₂O₄ and Ir–NiCo₂O₄ NSs for OER at 10 mA cm⁻² in 0.5 M H₂SO₄. f) The p–d orbital alignment of surface Ni, Co, and Ir sites for Ir–NiCo₂O₄-V₀. e, f) Reproduced with permission.^[80] Copyright 2020, American Chemical Society. g) Overpotentials at 10 mA cm⁻² (left) and Tafel slope (right) for ⁵⁷Au/NiFe LDH and pure NiFe LDH. h) Raman spectra of ⁵⁷Au/NiFe LDH at different potentials during CV scanning. g, h) Reproduced with permission.^[77] Copyright 2018, American Chemical Society. i) OER polarization curves of Co_xO_y and Co_xO_y. Reproduced with permission.^[84] Copyright 2020, The Authors, published by National Academy of Sciences USA. j) OER polarization curves of Fe_x(OH)_y/P-C and control samples. k) OER reaction pathway on Fe_x(OH)_y/P-C. l) Free energy diagram of OER on Fe_x(OH)_y/P-C and FeOOH. j–l) Reproduced with permission.^[85] Copyright 2021, American Chemical Society.

relatively high current density of 100 mA cm^{-2} with only $\approx 3.7\%$ of activity decay after 350 h, much better than those of Ir₁/NFH ($\approx 3.6\%$ decay after 198 h), Ir/C ($\approx 4\%$ decay after 25 h), and IrO₂ ($\approx 4\%$ decay after 25 h). These comparisons suggested that the NFS substrate could significantly improve the electrochemical kinetics and stability of Ir SAs relative to NFH. Simulation of the OER process by DFT illustrated that the maximum Gibbs free energy changes (ΔG_{max}) for both Ir₁/NFS and Ir₁/NFH correspond to the *O to *OOH conversion (Figure 10c,d) and importantly the ΔG_{max} for Ir₁/NFS (1.50 eV) was calculated to be smaller than that of Ir₁/NFH (1.59 eV) even under relatively low overpotential (0.27 vs 0.36 V), indicating the higher OER activity of Ir₁/NFS. PDOS and differential charge analysis indicated that the Ir SAs on sulfide substrates favored the loss of fewer electrons and exhibited a lower valence, leading to the relatively weaker coupling between Ir atoms and oxygen-containing intermediates, and thus lower energy barrier of the rate-limiting step.

Recently, Xi and co-workers prepared the Ir SAs on NiCo LDH (Ir–NiCo₂O₄ NSs) with oxygen vacancies as a stable electrocatalyst for acidic OER (0.5 M H₂SO₄).^[80] As shown in Figure 10e inset, the polarization curves displayed a low η_{10} of 240 mV for Ir–NiCo₂O₄ NSs, which is much smaller than those of commercial IrO₂ (370 mV) and NiCo₂O₄ NSs (>600 mV), suggesting the promoted OER performance. The smallest Tafel slope of Ir–NiCo₂O₄ NSs (60 mV dec^{−1}) compared to IrO₂ (80 mV dec^{−1}) and NiCo₂O₄ NSs (144 mV dec^{−1}) further illustrated the fastest OER kinetics. Strikingly, the Ir–NiCo₂O₄ NSs showed exceptional stability of acidic OER for about 70 h at 10 mA cm^{-2} with slight potential increase from 1.44 to 1.47 V vs RHE (Figure 10e), while the bare NiCo₂O₄ NSs can only sustain for several hours (<10 h). A series of physiochemical characterizations for the post-OER sample revealed the slight acid corrosion of Ni/Co species and well-maintained composition, morphology, and electronic structure. Combined XPS, EPR, and XAS measurements demonstrated the higher surface coupling of Ir–O_x species, bigger coordination number of Co–O, and higher oxygen vacancies (V_O) concentrations in Ir–NiCo₂O₄ NSs. PDOS analysis suggested that Ir sites noticeably enhance the electronic activity of surface lower coordinated Co sites for efficient electron exchange and transfer via shifting the d-band center toward Fermi level (E_{F}), and the almost unchanged Ni sites stabilize the valence states of Co sites. Consequently, both the Ir 5d-band and Co 3d-band exhibited excellent overlapping with H₂O 2p π and H 1s orbitals (Figure 10f) and thus optimal intermediates adsorption and electron transfer, yielding efficient OER. DFT computations showed that the maximum Gibbs free energy change for *O to *OOH conversion (ΔG_{max}) under $U = 1.23 \text{ V}$ can be reduced from 0.65 to 0.17 eV after Ir SAs incorporation, which can lower the energy barrier of initial water splitting to form *OH from 0.27 to 0.12 eV, and promote OER kinetics of Ir–NiCo₂O₄ NSs.

Besides accessing Ir SAs on transition-metal (hydr)oxides for OER, other noble-metal-based SAs like Ru and Au were also explored. For example, Zhang and co-workers directly electrodeposited Au SAs on NiFe LDH (^sAu/NiFe LDH) for improved OER and gained a fundamental understanding of the enhanced origin at the atomic level.^[77] Electrochemical testing illustrated that the η_{10} for ^sAu/NiFe LDH can be

reduced from 263 mV for NiFe LDH to 237 mV, along with the decreased Tafel slope (Figure 10g). Furthermore, the current density on ^sAu/NiFe LDH at an overpotential of 280 mV can reach 129.8 mA cm^{-2} , about 6 times higher than that on NiFe LDH (21.5 mA cm^{-2}). DFT simulations disclosed an overpotential of 0.18 V for the rate-limiting step of *O to *OOH conversion on ^sAu/NiFe LDH, in sharp contrast to that of 0.26 eV for the rate-limiting step of *OH to *O on NiFe LDH, highlighting the vital role of dispersing Au SAs on NiFe LDH in improving OER activity. Encouraged by the electrochemistry and DFT results, the authors performed in situ Raman spectroscopy measurements and a set of Raman spectra for ^sAu/NiFe LDH were collected under the applied potentials during CV scanning from 1.12 to 1.44 to 1.12 V (Figure 10h). During the anodic scanning from 1.12 to 1.32 V, the peaks at 462 and 535 cm^{−1} assignable to Ni–O vibrations of NiFe LDH can be observed. Further increasing the potential to 1.44 V, wherein the OER occurred, the primary two peaks disappeared and new peaks at 475 and 559 cm^{−1} attributed to characteristic bands in NiOOH emerged even when the potential was swept back to 1.12 V, indicative of the irreversible transformation from LDH into oxyhydroxides under the oxygen evolution potential which was also reinforced by ex situ XANES spectra of post-OER ^sAu/NiFe LDH. Differential charge analysis suggested that Au dz² orbital and O p_z orbital hybridization induces a net Au-to-LDH charge redistribution of 0.32 e, which transfers to surrounding O, Ni and Fe atoms, thus facilitating the adsorption of OH[−], O*, and OOH* intermediates to lower the overpotential of rate-limiting step for improved OER.

Nonprecious-metal-based SASCs have also been discovered for OER. Recently, Bard's group reported the direct electrodeposition (DED) of isolated cobalt oxide single molecules (Co₁O_x) as well as clusters (Co_nO_y) with diverse diameters on carbon fiber UME and investigated their size-dependent OER kinetics.^[84] As shown in Figure 10i, the polarization curves displayed the lowest overpotential for Co₁O_x, indicating the fastest rate. Increasing the size resulted in inferior OER performance (larger overpotential) and the difference in overpotential between the smallest and largest clusters was calculated to be about 120 mV. The authors proposed that Co(IV) is the active site, the per unit area of which become less available as the cluster size increases due to the limited exposure under the surface layer. They also noted that the intrinsic structure of different sized-clusters may also leads to distinct OER activities. Similarly, Zeng and co-workers directly electrodeposited Fe SAs based catalysts on porous carbon (Fe₁(OH)_x/P-C) for superb OER (Figure 10j–l).^[85] The polarization curve of the Fe₁(OH)_x/P-C demonstrated the smallest η_{10} (320 mV), and larger catalytic current than those of FeOOH, Fe₂O₃, and even commercial IrO₂ benchmark (370 mV). At an overpotential of 350 mV, the TOF of Fe₁(OH)_x/P-C was calculated to be 0.62 s^{-1} , 155-fold higher than that of FeOOH. Additionally, the mass activity of Fe₁(OH)_x/P-C ($4.30 \text{ A mg}_{\text{Fe}}^{-1}$) was estimated to be 143- and 358-fold higher than those of FeOOH ($0.030 \text{ A mg}_{\text{Fe}}^{-1}$) and commercial Fe₂O₃ ($0.012 \text{ A mg}_{\text{Fe}}^{-1}$), respectively. Differential pulse voltammogram (DPV) measurements revealed the presence of Fe³⁺/Fe²⁺ and Fe⁴⁺/Fe³⁺ redox couples for Fe₁(OH)_x/P-C, while the control FeOOH showed the existence of only Fe³⁺/Fe²⁺ couple at more positive potential. This comparison implied the

stronger tendency of $\text{Fe}_1(\text{OH})_x/\text{P-C}$ to transfer electrons. Since the oxidation of Fe^{3+} to Fe^{4+} in $\text{Fe}_1(\text{OH})_x/\text{P-C}$ occurred at a potential lower than the equilibrium potential of OER (1.23 V), the authors believed that the Fe^{4+} species in deed act as active sites for OER (Figure 10k), contrast to that of Fe^{3+} for FeOOH . DFT calculations further revealed that this facile Fe^{3+} to Fe^{4+} transformation for $\text{Fe}_1(\text{OH})_x/\text{P-C}$ is ascribed to the strong interaction between the Fe center and the P-C substrate via C–O–Fe bonding which shifts the Fe 3d and O 2p orbitals, and hence provides suitable adsorption sites for OER intermediates. The Gibbs free energy diagram illustrated that the rate-limiting step for both $\text{Fe}_1(\text{OH})_x/\text{P-C}$ and FeOOH is the $^*\text{O}$ to $^*\text{OOH}$ conversion. Compared with the Fe^{3+} active sites of FeOOH , the high-valent Fe^{4+} of $\text{Fe}_1(\text{OH})_x/\text{PC}$ elevated the electrophilicity of the $^*\text{O}$ intermediate, which favors the nucleophilic attack of OH^- to form $^*\text{OOH}$. Consequently, the energy barrier of rate-limiting step for $\text{Fe}_1(\text{OH})_x/\text{P-C}$ (1.57 eV) was significantly lower than that of FeOOH (2.97 eV, Figure 10l).

4.3. Overall Water Splitting (OWS)

A traditional water electrolyzer necessitates both HER and OER electrocatalysts under an identical electrolyte, which are commonly based on different materials, such that individual synthetic processes/equipment are needed.^[121] Using bifunctional electrocatalysts with both HER and OER activity to achieve overall water splitting (OWS) has advantages of simplifying the preparation procedures and lowering the overall manufacture cost.^[7,99,122–126]

Hou and co-workers realized a single SASC for OWS based on Ru SAs stabilized by defective nickel–iron LDH nanosheets ($\text{Ru}_1/\text{D-NiFe LDH}$).^[81] By intentional introduction and etching of Al species, the local coordination environments of catalytically active sites and the defects for $\text{Ru}_1/\text{D-NiFe LDH}$ can be precisely regulated for efficient HER and OER in same electrolyte (1.0 M KOH). As shown in Figure 11a, the $\text{Ru}_1/\text{D-NiFe LDH}$ exhibited a near-zero onset potential and greater catalytic

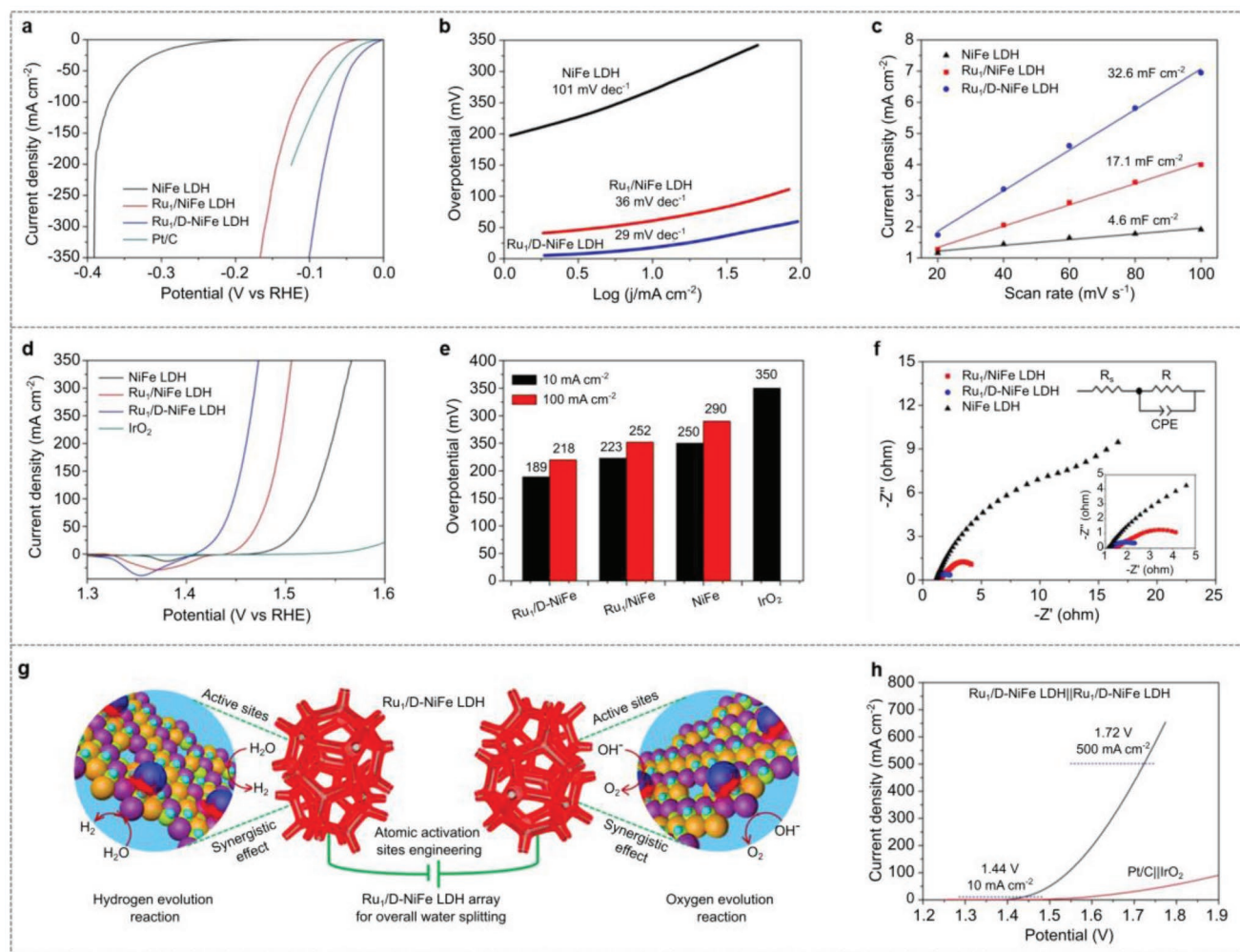


Figure 11. a) HER polarization curves, b) Tafel plots, c) scan-rate dependence of the current densities, d) OER polarization curves, e) overpotentials at typical current densities, and f) Nyquist plots of NiFe LDH, $\text{Ru}_1/\text{NiFe LDH}$, and $\text{Ru}_1/\text{D-NiFe LDH}$. Commercial Pt/C or IrO_2 are also included for comparison. g) Schematic diagram and h) polarization curves of overall water splitting catalyzed by $\text{Ru}_1/\text{D-NiFe LDH}$ couple, and commercial Pt/C|| IrO_2 couple are also included for comparison. a–h) Reproduced under the terms of the CC-BY Creative Commons Attribution 4.0 International license (<https://creativecommons.org/licenses/by/4.0/>).^[81] Copyright 2021, The Authors, published by Springer Nature.

current for HER in comparison to those of NiFe LDH, Ru₁/NiFe LDH, and Pt/C benchmark, manifesting the positive effects of Ru SAs and defects. For example, Ru₁/D-NiFe LDH required the overpotentials of only 18 and 61 mV to deliver 10 and 100 mA cm⁻², respectively, lower than those of Pt/C (33 and 90 mV), Ru₁/NiFe LDH (62 and 118 mV), and NiFe LDH (272 and 371 mV). The low Tafel slope of Ru₁/D-NiFe LDH (29 mV dec⁻¹) compared to those of Ru₁/NiFe LDH (26 mV dec⁻¹) and NiFe LDH (101 mV dec⁻¹) further substantiated its outstanding HER kinetics (Figure 11b) and suggested the Volmer–Tafel mechanism. Interestingly, a notable mass activity of 14650 A g_{metal}⁻¹ for Ru₁/D-NiFe LDH was achieved at the overpotential of 100 mV, which is ≈7 times higher than that of Ru₁/NiFe LDH (2420 A g_{metal}⁻¹), and ≈45 times higher than that of Pt/C (320 A g_{metal}⁻¹). To further understand the improved HER performance of Ru₁/D-NiFe LDH in comparison to those controls, the electrochemically active surface areas (ECSAs) were estimated from the electrochemical double-layer capacitance (C_{dl}) by collecting cyclic voltammograms in a non-Faradaic region.^[127,128] Figure 11c clearly demonstrated the highest C_{dl} of Ru₁/D-NiFe LDH (32.6 mF cm⁻²), 1.9- and 1.7-fold higher than those of Ru₁/NiFe LDH and NiFe LDH, respectively. The high ECSA of Ru₁/D-NiFe LDH enabled the effective accessibility of active sites and thus promoted HER, as further verified by the small charge-transfer resistance via EIS measurements. DFT modeling illustrated that the Gibbs free energy changes for hydrogen adsorption (ΔG_{H*}) at the Ru site of Ru₁/D-NiFe LDH (0.25 eV) is lower than those at Ni (1.53 eV) and Fe (1.16 eV) sites, indicating Ru sites as the active center. Apart from higher HER activity, polarization curves before and after 2000 cycles, and chronopotentiometry tests for Ru₁/D-NiFe LDH showed little changes, indicative of the excellent long-term durability.

The OER performance of the Ru₁/D-NiFe LDH along with control samples were also evaluated in 1.0 M KOH (Figure 11d–f). As shown in Figure 11d,e, the Ru₁/D-NiFe LDH afforded 10 and 100 mA cm⁻² at low overpotentials of 189 and 220 mV, respectively, substantially lower than those of NiFe LDH (250 and 290 mV) and commercial IrO₂ (350 mV), demonstrating its remarkable OER activity. The steep polarization curve of Ru₁/D-NiFe LDH near the onset potential suggested the low Tafel slope (31 mV dec⁻¹) and thus fast OER kinetics. Also, the Nyquist plot of Ru₁/D-NiFe LDH exhibited a smaller semicircle diameter than those of Ru₁/NiFe LDH and NiFe LDH (Figure 11f), implying the faster charge transfer between the electrodes and the electrolyte. Particularly, the mass activity of Ru₁/D-NiFe LDH was calculated to be high as 11980 A g_{metal}⁻¹ at an overpotential of 240 mV. DFT calculations illustrated the rate-limiting step for Ru₁/D-NiFe LDH (Ru–O as the active site) is the formation of *OH with an energy uphill of 0.38 eV, which is significantly lower than those for Ni–O and Fe–O sites in NiFe LDH. Thus, both experiment and theoretical simulation confirmed that the Ru SAs and defects of NiFe LDH synergistically accelerate the reactive kinetics for both the HER and OER in the same electrolyte.

Inspired by the superior bifunctionality of Ru₁/D-NiFe LDH, the authors assembled a two-electrode electrolyzer using Ru₁/D-NiFe LDH as both anode and cathode for overall water splitting (Figure 11g).^[81] the polarization curve of Ru₁/D-NiFe

LDH couple required low cell voltages of 1.44 and 1.54 V to reach 10 and 100 mA cm⁻², respectively, even better than that of Pt/C-IrO₂ couple (Figure 11h). Strikingly, the Ru₁/D-NiFe LDH couple can afford the industrial current density as high as 500 mA cm⁻² at a low cell voltage of only 1.72 V, along with robust durability at 10 and 100 mA cm⁻² for 100 h.

4.4. Oxygen Reduction Reaction (ORR)

Closing the green hydrogen cycling needs advanced devices to utilize the hydrogen generated from water splitting. Among them, the hydrogen–oxygen fuel cell is one of the most promising examples of hydrogen utilization equipment.^[20,129] However, its overall efficiency is severely hindered by the sluggish electrode reactions, especially the cathodic oxygen reduction reaction (ORR).^[130–132] As the reverse reaction of OER, ORR also contains four-electron-proton-transfer process with high reactive energy barriers, such that a large amount of Pt-based catalyst is usually needed, posing prohibitive cost for the large-scale commercialization.^[19,20,129,133] It is thus desirable to develop high-performance and cost-effective low Pt or non-Pt catalysts for ORR.^[134] SASCs with high activity and atomic efficiency have the possibility to achieve this goal.

Yao and co-workers reported that atomically dispersed Pt–Co on a nitrogen–carbon support (A-CoPt-NC) can serve as an advanced ORR electrocatalyst with high activity and four-electron selectivity (Figure 12).^[93] Noise-filtered HAADF STEM imaging identified the local coordination of the metal atoms (Figure 12a,b), wherein the metal atoms linked by the adjacent carbon/nitrogen atoms were featured with purple circles (Figure 12c).

The electrocatalytic ORR performance of A-CoPt-NC was studied by steady-state LSV on a rotating disk electrode (RDE) at different rotating speeds in O₂-saturated 0.1 M KOH electrolyte. As shown in Figure 12d, all the steady-state ORR polarization curves of A-CoPt-NC exhibited well-defined diffusion-limiting currents (0.4–0.8 V vs RHE) following a mixed kinetic-diffusion region. Moreover, linearity of Koutecký–Levich (K–L) plots and the near parallelism of the fitting lines suggested the first-order reaction kinetics with respect to dissolved O₂ and potential-independent electron-transfer number.^[135] The slopes of the K–L plots revealed a four electron (n = 4) ORR pathway. To emphasize the eminent activity of A-CoPt-NC, two controls of Co-NC and commercial Pt/C benchmark were also tested for comparison. Figure 12e exhibited that the Co-NC possesses a higher half-wave potential (0.92 V vs RHE) but lower limiting current density (4.8 mA cm⁻²) than those of Pt/C. Remarkably, the A-CoPt-NC demonstrated the best performance among them, as reflected by the most positive half-wave potential (0.96 V vs RHE) and largest limiting current density (≈5.8 mA cm⁻²), demonstrating the synergistic effect induced by the SAs of Pt and Co. Moreover, the mass activity of A-CoPt-NC (45.47 A mg⁻¹) was calculated to be 267 times higher than that of Pt/C (0.17 A mg⁻¹). Also, its specific activity and TOF were 3-fold and 81-fold greater than those of Pt/C, respectively (Figure 12f).^[93] In addition, the A-CoPt-NC exhibited excellent durability with 96.4% activity retain, better than that for Pt/C (79.7%). The rotating ring disk electrode (RRDE) tests

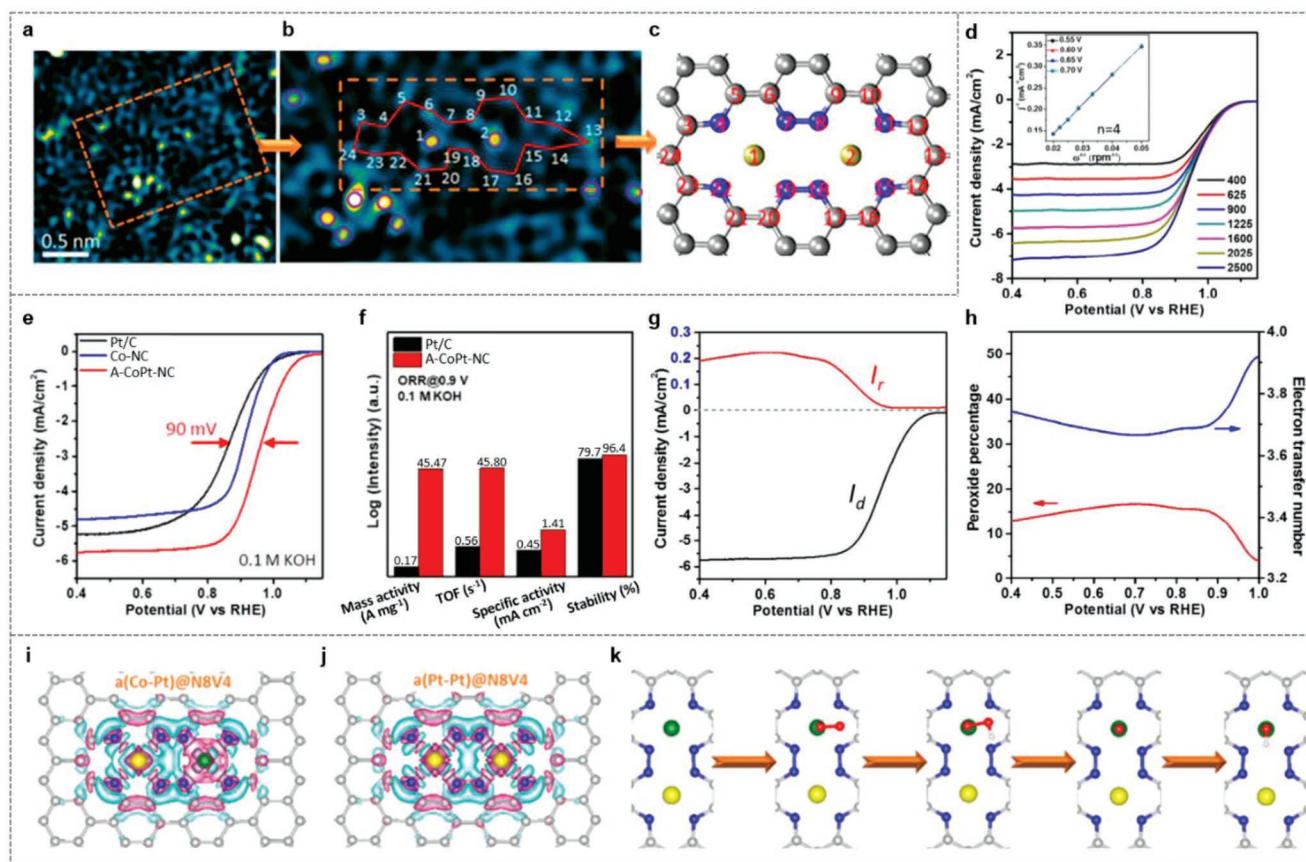


Figure 12. a) HAADF and b) the corresponding zoomed-in image of A-CoPt-NC. The bright yellow and cyan spots are metal atoms and carbon atoms, respectively. c) Model of the two metal atoms trapped in the defect. d) RDE polarization curves of A-CoPt-NC at different rotating speeds in O₂-saturated 0.1 M KOH solution. The inset shows the corresponding K-L plots at different potentials. e) RDE polarization curves of Co-NC, A-CoPt-NC, and Pt/C for ORR. f) Comparison of mass activity, TOF, specific activity, and stability of the A-CoPt-NC and Pt/C for ORR. g) Rotating ring-disk electrode voltammogram of A-CoPt-NC at a rotation rate of 1600 rpm. h) The corresponding percentage of peroxide and the electron transfer number of A-CoPt-NC for ORR. i, j) Top views of the charge densities of a(Co-Pt)@N8V4 (i) and a(Pt-Pt)@N8V4 (j). k) The ORR reaction pathway on a(Co-Pt)@N8V4. a–k) Reproduced with permission.^[93] Copyright 2018, American Chemical Society.

(Figure 12g,h) also showed a high electron-transfer number above 3.6 and a low H₂O₂ yield below 17% for A-CoPt-NC over the potential window from 0.4 to 1.0 V versus RHE, confirming the predominant four-electron ORR pathway.

The authors speculated that the synergetic effect of atomic Pt–Me (Me = Co/Pt) coupling species at the carbon defects (denoted as a(Pt–Me)@Defects) in A-CoPt-NC accounts for the superb ORR performance. Based on the structural observations (Figure 12a–c) and XANES fittings, two representative models of a(Co–Pt)@N8V4 and a(Co–Pt)@N6V4 were constructed (Figure 12i,j), and thus the corresponding Gibbs free energy diagram for ORR over the two models can be obtained. The results revealed that the most energetically favorable configuration is a(Co–Pt)@N8V4 with a low overpotential of 0.30 V for the rate-limiting step (the first protonation, O₂→OOH*). In contrast, the corresponding overpotential over a(Pt–Pt)@N8V4 was high to 1.07 V. DOS analysis implied that the Co 3d orbital in a(Co–Pt)@N8V4 is much closer to the Fermi level than that of the Pt 5d orbital in a(Pt–Pt)@N8V4, indicating the strong binding with oxygen for the former. Additionally, the stronger electron accumulation (pink area) around the Co atom in a(Co–Pt)@N8V4 relative to that around Pt in a(Pt–Pt)@

N8V4 (Figure 12i,j) can further accelerate the reduction of O₂ (Figure 12k), leading to enhanced ORR performance.

5. Conclusion and Perspective

With benign synthetic conditions, simple processing steps, and short preparation time, ambient electrocatalysis has established a novel and effective avenue for the rapid synthesis of catalysts with single-atom sites (SASs) for electrocatalytic green hydrogen cycling. Herein, we have summarized recent achievements in ambient electrocatalysis toward SASs ranging from nonprecious metals such as Fe, Co, Ni, Cu, Zn, V, Cr, Mn, Sn, Pb, Bi to noble-metals including Ru, Rh, Pd, Ag, Ir, Pt, and Au, some of which have exhibited excellent electrocatalytic performance for hydrogen generation from water splitting and oxidative conversion through a hydrogen–oxygen fuel cell to achieve hydrogen economy. Specifically, these ambient electrocatalysis methodologies include top-down electrochemical etching (ECE) that gradually etches bulk metal counterparts away to leave single atoms, bottom-up direct electrodeposition (DED), which generates single atoms directly from metal ion solutions with

applied currents or potentials, and combined top-down and bottom-up electrochemical leaching–redeposition (ELR), which contains first electrochemical leaching of bulk metals followed by deposition onto counter substrates to access SASs. Although great progress has been made, we are still facing some challenges and there is a long way ahead for the facile and affordable synthesis of high-performance SAS-based catalysts (SASCs) to electrochemically produce and convert hydrogen in a sustainable manner.

First, although ambient electrosynthesis is simple and environmentally benign, it usually obtains SASs on a specific substrate with a small geometric area ($<1\text{ cm}^2$) in an H-type or single compartment cell, such synthetic configuration and the resulting SASs-loaded electrodes are perfect for electrocatalytic measurements in laboratory, while for practical membrane electrode assemblies (MEAs) or even device fabrications, it is required to expand the electrosynthesis scale and little attention has been paid currently. Simple and proportional scale-up would fail due to the suffered mass and heat transfer limitation at high currents/potentials in an H-cell. Developing novel electrolyzers and supporting electrodes with hierarchical porosity for rapid ion transport is desirable. The multichannel flow reactor system can overcome the mass/heat transport limitations by continuously circulating the precursors' solutions and products to and away from the electrodes,^[136] rendering it potentially effective for large-scale synthesis of SASs. Due to the high propensity of single atoms to aggregate, the resulting SASs prepared by a vast majority of strategies including ambient electrosynthesis normally possess low metal loading ($<5\text{ wt}\%$, Table 1), leading to low volumetric density of active sites in SASs relative to that of traditional nanocrystal catalysts. It is thus essential to increase the mass loading and/or availability of SASs. Tailoring the morphology of the supports with 3D open porous architectures, plentiful defects and strong coordination atoms would not only improve the accessibility of active sites but also provide adequate anchoring sites to stabilize single atoms, such that diverse nanostructure and electronic state engineering like 3D-printing, shape-controlled synthesis, interfacing, and plasma activation are welcome.^[137] Additionally, because only the surface species of the supports accounts for anchoring SASs, repeated sequential deposition of supports and SASs is good for the construction of MEAs with laminate structure to maximize the loading of SASs.

Second, SASs ideally feature with well-defined coordination structures, which would facilitate exploring the structure–electrocatalytic mechanism correlations, while current physiochemical characterizations like XAS can only show us the statistical or proximate structure. For instance, most XAS analyses mainly focus on the first coordination shell of SASs. Very few studies investigate their second or higher coordination shells due to the complex interaction between the X-rays and the underlying materials. High-resolution electron microscopy can directly evidence the atomic dispersion of SASs with 2D imaging, while thorough description of their 3D spatial configurations has remained limited. Novel, rapid, and nondestructive 3D tomography combined with intelligent massive data analysis system such as machine learning is desirable. Notably, some in situ/operando techniques have revealed the dynamic evolution or even reconstruction of SASs during the electrocatalytic

processes,^[138–140] meaning that the original SASs confirmed by ex situ physiochemical characterizations may not be the real active centers. Moreover, each characterization technique has its own limitations in terms of the detection range, it seems impossible that one or few analytical techniques can give us a full picture of what happens for the whole electrocatalysis process which may be governed by multiple factors including the oxidation state and local coordination structure of SASs, and electrolyte–electrode interface. Consequently, innovative characterization techniques and their combination are demanded for real-time and comprehensive monitoring of the SASs-catalyzed reactive interfaces. Theory modulations like DFT are beneficial to help us to in-depth understand the origin of dynamic changes of SASs and the underlying electrocatalytic mechanism, while the prevailing modeling based on the local coordination of central metal atoms (first coordination shell) is too simple in some cases, because recent work has showed that the adjacent SASs exhibit new electronic properties and electrocatalytic behaviors.^[93,141] Introducing machine learning to accurately construct the models close to real reaction interfaces would greatly promote the discovery of next-generation descriptor-based approaches to screen and guide the design of advanced SASs.

Third, in spite of the fact that SASs have showed exceptional activity and stability for HER, OER, and ORR, closing the green hydrogen cycling needs high-performance electrocatalysts for the hydrogen oxidation reaction (HOR), an anode half-reaction in the hydrogen-oxidation fuel cell.^[142–144] Although HOR with two-electron–proton transfer is thermodynamically more favorable than ORR, the kinetics, even for the state-of-the-art Pt catalysts in alkaline electrolyte, is still sluggish.^[145] Considering the marvelous properties of SASs, it is worthy to extend their application in HOR. However, to our knowledge, relevant researches have been rarely reported. It is therefore urgent and important to precisely design advanced SASs on the basis of ambient electrosynthesis for HOR electrocatalysis.

Finally, given the flowing characters of commercial-scale water electrolyzers and fuel cells, it is encouraged to further evaluate the performance of SASs in real working conditions, not only in H-cells due to the fact that direct incorporation of SASs into MEAs or devices following the established paradigms may face new challenges in water management, reactants/products transfer and components assembly. Separately investigating individual components within a device or system is obviously insufficient,^[146] and system materials and advanced manufacturing engineering is therefore needed to comprehensively study the interactions between individual components and how these interactions result in the whole performance of the final system.

Supporting Information

Supporting Information is available from the Wiley Online Library or from the author.

Acknowledgements

This work was supported by The National Key Research and Development Program of China (2021YFA1600800), the Start-up Funding of the Huazhong University of Science and Technology (HUST), the Program

for HUST Academic Frontier Youth Team, The Innovation and Talent Recruitment Base of New Energy Chemistry and Device (B21003), the Open Research Fund of Key Laboratory of Material Chemistry for Energy Conversion and Storage (HUST), Ministry of Education (2021JYBK03), the Open Fund of Hubei Key Laboratory of Material Chemistry and Service Failure, Huazhong University of Science and Technology (2020MCF03), the Open Research Fund of Key Laboratory of Green and Precise Synthetic Chemistry and Applications, Ministry of Education, Huaibei Normal University (2020KF05), the Hainan Provincial Joint Project of Sanya Yazhou Bay Science and Technology City (520LH054), The Fundamental Research Funds for the Central Universities (WUT: 2021IVA66), Wuhan University of Technology Startup Fund (40120562), and the National Natural Science Foundation of China (22075092).

Conflict of Interest

The authors declare no conflict of interest.

Keywords

ambient electrosynthesis, electrocatalysis, fuel cells, single-atom sites, water splitting

Received: November 17, 2022

Published online:

- [1] C. Gao, J. Low, R. Long, T. Kong, J. Zhu, Y. Xiong, *Chem. Rev.* **2020**, *120*, 12175.
- [2] N. C. S. Selvam, L. Du, B. Y. Xia, P. J. Yoo, B. You, *Adv. Funct. Mater.* **2021**, *31*, 2008190.
- [3] S. Chu, Y. Cui, N. Liu, *Nat. Mater.* **2017**, *16*, 16.
- [4] R. Sun, Y. Liao, S.-T. Bai, M. Zheng, C. Zhou, T. Zhang, B. F. Sels, *Energy Environ. Sci.* **2021**, *14*, 1247.
- [5] J. A. Turner, *Science* **2004**, *305*, 972.
- [6] S. Chu, A. Majumdar, *Nature* **2012**, *488*, 294.
- [7] B. You, Y. Sun, *Acc. Chem. Res.* **2018**, *51*, 1571.
- [8] I. Roger, M. A. Shipman, M. D. Symes, *Nat. Rev. Chem.* **2017**, *1*, 0003.
- [9] J. O. Bockris, *Int. J. Hydrogen Energy* **2002**, *27*, 731.
- [10] N. M. Dowell, N. Sunny, N. Brandon, H. Herzog, A. Y. Ku, W. Maas, A. Ramirez, D. M. Reiner, G. N. Sant, N. Shah, *Joule* **2021**, *5*, 2524.
- [11] I. Staffell, D. Scamman, A. Velazquez Abad, P. Balcombe, P. E. Dodds, P. Ekins, N. Shah, K. R. Ward, *Energy Environ. Sci.* **2019**, *12*, 463.
- [12] Z.-Y. Yu, Y. Duan, X.-Y. Feng, X. Yu, M.-R. Gao, S.-H. Yu, *Adv. Mater.* **2021**, *33*, 2007100.
- [13] M. van der Spek, C. Banet, C. Bauer, P. Gabrielli, W. Goldthorpe, M. Mazzotti, S. T. Munkejord, N. A. Røkke, N. Shah, N. Sunny, D. Sutter, J. M. Trusler, M. Gazzani, *Energy Environ. Sci.* **2022**, *15*, 1034.
- [14] X. Zhao, L. Du, B. You, Y. Sun, *Catal. Sci. Technol.* **2020**, *10*, 2711.
- [15] Y. Luo, Y. Wu, C. Huang, C. Menon, S.-P. Feng, P. K. Chu, *EcoMat* **2022**, *4*, e12197.
- [16] X. Zou, Y. Zhang, *Chem. Soc. Rev.* **2015**, *44*, 5148.
- [17] M. Chatenet, B. G. Pollet, D. R. Dekel, F. Dionigi, J. Deseure, P. Millet, R. D. Braatz, M. Z. Bazant, M. Eikerling, I. Staffell, P. Balcombe, Y. Shao-Horn, H. Schäfer, *Chem. Soc. Rev.* **2022**, *51*, 4583.
- [18] Z. W. Seh, J. Kibsgaard, C. F. Dickens, I. Chorkendorff, J. K. Nørskov, T. F. Jaramillo, *Science* **2017**, *355*, eaad4998.
- [19] X. X. Wang, M. T. Swihart, G. Wu, *Nat. Catal.* **2019**, *2*, 578.
- [20] M. Shao, Q. Chang, J.-P. Dodelet, R. Chenitz, *Chem. Rev.* **2016**, *116*, 3594.
- [21] a) T. Wu, E. Song, S. Zhang, M. Luo, C. Zhao, W. Zhao, J. Liu, F. Huang, *Adv. Mater.* **2022**, *34*, 2108505; b) Y. Zhao, W. J. Jiang, J. Zhang, E. C. Lovell, R. Amal, Z. Han, X. Lu, *Adv. Mater.* **2021**, *33*, 2102801.
- [22] D. Zhao, Z. Zhuang, X. Cao, C. Zhang, Q. Peng, C. Chen, Y. Li, *Chem. Soc. Rev.* **2020**, *49*, 2215.
- [23] V. R. Stamenkovic, D. Strmcnik, P. P. Lopes, N. M. Markovic, *Nat. Mater.* **2016**, *16*, 57.
- [24] C. Xie, Z. Niu, D. Kim, M. Li, P. Yang, *Chem. Rev.* **2020**, *120*, 1184.
- [25] X. F. Yang, A. Wang, B. Qiao, J. Li, J. Liu, T. Zhang, *Acc. Chem. Res.* **2013**, *46*, 1740.
- [26] Y. Chen, J. Lin, B. Jia, X. Wang, S. Jiang, T. Ma, *Adv. Mater.* **2022**, *34*, 2201796.
- [27] a) A. Wang, J. Li, T. Zhang, *Nat. Rev. Chem.* **2018**, *2*, 65; b) Z. Chen, J. Liu, M. J. Koh, K. P. Loh, *Adv. Mater.* **2022**, *34*, 2103882.
- [28] C. Xia, Y. Qiu, Y. Xia, P. Zhu, G. King, X. Zhang, Z. Wu, J. Y. Kim, D. A. Cullen, D. Zheng, P. Li, M. Shakouri, E. Heredia, P. Cui, H. N. Alshareef, Y. Hu, H. Wang, *Nat. Chem.* **2021**, *13*, 887.
- [29] Y. Chen, S. Ji, C. Chen, Q. Peng, D. Wang, Y. Li, *Joule* **2018**, *2*, 1242.
- [30] L. Li, X. Chang, X. Lin, Z.-J. Zhao, J. Gong, *Chem. Soc. Rev.* **2020**, *49*, 8156.
- [31] H. Xu, D. Cheng, D. Cao, X. C. Zeng, *Nat. Catal.* **2018**, *1*, 339.
- [32] a) R. T. Hannagan, G. Giannakakis, M. Flytzani-Stephanopoulos, E. C. H. Sykes, *Chem. Rev.* **2020**, *120*, 12044; b) W. Guo, Z. Wang, X. Wang, Y. Wu, *Adv. Mater.* **2021**, *33*, 2004287.
- [33] X. Cui, W. Li, P. Ryabchuk, K. Junge, M. Beller, *Nat. Catal.* **2018**, *1*, 385.
- [34] F. Chen, X. Jiang, L. Zhang, R. Lang, B. Qiao, *Chin. J. Catal.* **2018**, *39*, 893.
- [35] S. Mitchell, J. Pérez-Ramírez, *Nat. Commun.* **2020**, *11*, 4302.
- [36] a) Y. Li, S. L. Zhang, W. Cheng, Y. Chen, D. Luan, S. Gao, X. W. Lou, *Adv. Mater.* **2022**, *34*, 2105204; b) Y. Peng, B. Lu, S. Chen, *Adv. Mater.* **2018**, *30*, 201801995.
- [37] a) Y. Li, X. F. Lu, S. Xi, D. Luan, X. Wang, X. W. Lou, *Angew. Chem., Int. Ed.* **2022**, *61*, e202201491; b) X. Sun, L. Sun, G. Li, Y. Tuo, C. Ye, J. Yang, J. Low, X. Yu, J. H. Bitter, Y. Lei, D. Wang, Y. Li, *Angew. Chem., Int. Ed.* **2022**, *61*, e202207677.
- [38] Y. Pan, R. Lin, Y. Chen, S. Liu, W. Zhu, X. Cao, W. Chen, K. Wu, W.-C. Cheong, Y. Wang, L. Zheng, J. Luo, Y. Lin, Y. Liu, C. Liu, J. Li, Q. Lu, X. Chen, D. Wang, Q. Peng, C. Chen, Y. Li, *J. Am. Chem. Soc.* **2018**, *140*, 4218.
- [39] Z. Zeng, L. Y. Gan, H. Bin Yang, X. Su, J. Gao, W. Liu, H. Matsumoto, J. Gong, J. Zhang, W. Cai, Z. Zhang, Y. Yan, B. Liu, P. Chen, *Nat. Commun.* **2021**, *12*, 4088.
- [40] Y. Jiao, Y. Zheng, P. Chen, M. Jaroniec, S.-Z. Qiao, *J. Am. Chem. Soc.* **2017**, *139*, 18093.
- [41] Z.-Y. Wu, M. Karamad, X. Yong, Q. Huang, D. A. Cullen, P. Zhu, C. Xia, Q. Xiao, M. Shakouri, F.-Y. Chen, J. Y. Kim, Y. Xia, K. Heck, Y. Hu, M. S. Wong, Q. Li, I. Gates, S. Siahrostami, H. Wang, *Nat. Commun.* **2021**, *12*, 2870.
- [42] H. Liu, X. Lang, C. Zhu, J. Timoshenko, M. Rüscher, L. Bai, N. Guijarro, H. Yin, Y. Peng, J. Li, Z. Liu, W. Wang, B. R. Cuenya, J. Luo, *Angew. Chem., Int. Ed.* **2022**, *61*, e202202556.
- [43] E. Murphy, Y. Liu, I. Matanovic, S. Guo, P. Tieu, Y. Huang, A. Ly, S. Das, I. Zenyuk, X. Pan, E. Spoecker, P. Atanassov, *ACS Catal.* **2022**, *12*, 6651.
- [44] Z. Geng, Y. Liu, X. Kong, P. Li, K. Li, Z. Liu, J. Du, M. Shu, R. Si, J. Zeng, *Adv. Mater.* **2018**, *30*, 1803498.
- [45] L. Hui, Y. Xue, H. Yu, Y. Liu, Y. Fang, C. Xing, B. Huang, Y. Li, *J. Am. Chem. Soc.* **2019**, *141*, 10677.
- [46] X. Liu, Y. Jiao, Y. Zheng, M. Jaroniec, S.-Z. Qiao, *J. Am. Chem. Soc.* **2019**, *141*, 9664.
- [47] Y. Lu, T. Liu, C.-L. Dong, Y.-C. Huang, Y. Li, J. Chen, Y. Zou, S. Wang, *Adv. Mater.* **2021**, *33*, 2007056.

- [48] Y. Wang, Y.-Q. Zhu, Z. Xie, S.-M. Xu, M. Xu, Z. Li, L. Ma, R. Ge, H. Zhou, Z. Li, X. Kong, L. Zheng, J. Zhou, H. Duan, *ACS Catal.* **2022**, *12*, 12432.
- [49] K. Ji, M. Xu, S.-M. Xu, Y. Wang, R. Ge, X. Hu, X. Sun, H. Duan, *Angew. Chem. Int. Ed.* **2022**, *61*, e202209849.
- [50] R. Ge, Y. Wang, Z. Li, M. Xu, S.-M. Xu, H. Zhou, K. Ji, F. Chen, J. Zhou, H. Duan, *Angew. Chem., Int. Ed.* **2022**, *61*, e202200211.
- [51] J. Jones, H. Xiong, A. T. DeLaRiva, E. J. Peterson, H. Pham, S. R. Challa, G. Qi, S. Oh, M. H. Wiebenga, X. I. P. Hernández, Y. Wang, A. K. Datye, *Science* **2016**, *353*, 150.
- [52] Y. Yao, Z. Huang, P. Xie, L. Wu, L. Ma, T. Li, Z. Pang, M. Jiao, Z. Liang, J. Gao, Y. He, D. J. Kline, M. R. Zachariah, C. Wang, J. Lu, T. Wu, T. Li, C. Wang, R. Shahbazian-Yassar, L. Hu, *Nat. Nanotechnol.* **2019**, *14*, 851.
- [53] S. Wei, A. Li, J.-C. Liu, Z. Li, W. Chen, Y. Gong, Q. Zhang, W.-C. Cheong, Y. Wang, L. Zheng, H. Xiao, C. Chen, D. Wang, Q. Peng, L. Gu, X. Han, J. Li, Y. Li, *Nat. Nanotechnol.* **2018**, *13*, 856.
- [54] Y. Qu, Z. Li, W. Chen, Y. Lin, T. Yuan, Z. Yang, C. Zhao, J. Wang, C. Zhao, X. Wang, F. Zhou, Z. Zhuang, Y. Wu, Y. Li, *Nat. Catal.* **2018**, *1*, 781.
- [55] P. Wang, Y. Ren, R. Wang, P. Zhang, M. Ding, C. Li, D. Zhao, Z. Qian, Z. Zhang, L. Zhang, L. Yin, *Nat. Commun.* **2020**, *11*, 1576.
- [56] L. Cao, W. Liu, Q. Luo, R. Yin, B. Wang, J. Weissenrieder, M. Soldemo, H. Yan, Y. Lin, Z. Sun, C. Ma, W. Zhang, S. Chen, H. Wang, Q. Guan, T. Yao, S. Wei, J. Yang, J. Lu, *Nature* **2019**, *565*, 631.
- [57] H. Yan, H. Cheng, H. Yi, Y. Lin, T. Yao, C. Wang, J. Li, S. Wei, J. Lu, *J. Am. Chem. Soc.* **2015**, *137*, 10484.
- [58] D. Liu, X. Li, S. Chen, H. Yan, C. Wang, C. Wu, Y. A. Haleem, S. Duan, J. Lu, B. Ge, P. M. Ajayan, Y. Luo, J. Jiang, L. Song, *Nat. Energy* **2019**, *4*, 512.
- [59] N. Cheng, S. Stambula, D. Wang, M. N. Banis, J. Liu, A. Riese, B. Xiao, R. Li, T.-K. Sham, L.-M. Liu, G. A. Botton, X. Sun, *Nat. Commun.* **2016**, *7*, 13638.
- [60] P. Liu, Y. Zhao, R. Qin, S. Mo, G. Chen, L. Gu, D. M. Chevrier, P. Zhang, Q. Guo, D. Zang, B. Wu, G. Fu, N. Zheng, *Science* **2016**, *352*, 797.
- [61] M. Yang, L. F. Allard, M. Flytzani-Stephanopoulos, *J. Am. Chem. Soc.* **2013**, *135*, 3768.
- [62] H. Wei, K. Huang, D. Wang, R. Zhang, B. Ge, J. Ma, B. Wen, S. Zhang, Q. Li, M. Lei, C. Zhang, J. Irawan, L.-M. Liu, H. Wu, *Nat. Commun.* **2017**, *8*, 1490.
- [63] Y. Qu, L. Wang, Z. Li, P. Li, Q. Zhang, Y. Lin, F. Zhou, H. Wang, Z. Yang, Y. Hu, M. Zhu, X. Zhao, X. Han, C. Wang, Q. Xu, L. Gu, J. Luo, L. Zheng, Y. Wu, *Adv. Mater.* **2019**, *31*, 1904496.
- [64] H. Fei, J. Dong, C. Wan, Z. Zhao, X. Xu, Z. Lin, Y. Wang, H. Liu, K. Zang, J. Luo, S. Zhao, W. Hu, W. Yan, I. Shakir, Y. Huang, X. Duan, *Adv. Mater.* **2018**, *30*, 1802146.
- [65] S. Ye, F. Luo, Q. Zhang, P. Zhang, T. Xu, Q. Wang, D. He, L. Guo, Y. Zhang, C. He, X. Ouyang, M. Gu, J. Liu, X. Sun, *Energy Environ. Sci.* **2019**, *12*, 1000.
- [66] a) X. Guo, G. Fang, G. Li, H. Ma, H. Fan, L. Yu, C. Ma, X. Wu, D. Deng, M. Wei, D. Tan, R. Si, S. Zhang, J. Li, L. Sun, Z. Tang, X. Pan, X. Bao, *Science* **2014**, *344*, 616; b) X. Cui, J. Xiao, Y. Wu, P. Du, R. Si, H. Yang, H. Tian, J. Li, W.-H. Zhang, D. Deng, X. Bao, *Angew. Chem., Int. Ed.* **2016**, *55*, 6708; c) X. Chen, L. Yu, S. Wang, D. Deng, X. Bao, *Nano Energy* **2017**, *32*, 353.
- [67] B. K. Peters, K. X. Rodriguez, S. H. Reisberg, S. B. Beil, D. P. Hickey, Y. Kawamata, M. Collins, J. Starr, L. Chen, S. Udyavara, K. Klunder, T. J. Gorey, S. L. Anderson, M. Neurock, S. D. Minteer, P. S. Baran, *Science* **2019**, *363*, 838.
- [68] H. Davy, *Philos. Trans. R. Soc. London* **1807**, *97*, 1.
- [69] C. Schotten, T. P. Nicholls, R. A. Bourne, N. Kapur, B. N. Nguyen, C. E. Willans, *Green Chem.* **2020**, *22*, 3358.
- [70] P. Sebastián-Pascual, I. Jordão Pereira, M. Escudero-Escribano, *Chem. Commun.* **2020**, *56*, 13261.
- [71] P. Ganesan, A. Sivanantham, S. Shanmugam, *J. Mater. Chem. A* **2016**, *4*, 16394.
- [72] L. Fan, P. F. Liu, X. Yan, L. Gu, Z. Z. Yang, H. G. Yang, S. Qiu, X. Yao, *Nat. Commun.* **2016**, *7*, 10667.
- [73] J. C. Liu, H. Xiao, J. Li, *J. Am. Chem. Soc.* **2020**, *142*, 3375.
- [74] M. Zhou, J. E. Dick, A. J. Bard, *J. Am. Chem. Soc.* **2017**, *139*, 17677.
- [75] M. Zhou, S. Bao, A. J. Bard, *J. Am. Chem. Soc.* **2019**, *141*, 7327.
- [76] K. L. Zhou, Z. Wang, C. B. Han, X. Ke, C. Wang, Y. Jin, Q. Zhang, J. Liu, H. Wang, H. Yan, *Nat. Commun.* **2021**, *12*, 3783.
- [77] J. Zhang, J. Liu, L. Xi, Y. Yu, N. Chen, S. Sun, W. Wang, K. M. Lange, B. Zhang, *J. Am. Chem. Soc.* **2018**, *140*, 3876.
- [78] Z. Zhang, C. Feng, C. Liu, M. Zuo, L. Qin, X. Yan, Y. Xing, H. Li, R. Si, S. Zhou, J. Zeng, *Nat. Commun.* **2020**, *11*, 1215.
- [79] Z. Lei, W. Cai, Y. Rao, K. Wang, Y. Jiang, Y. Liu, X. Jin, J. Li, Z. Lv, S. Jiao, W. Zhang, P. Yan, S. Zhang, R. Cao, *Nat. Commun.* **2022**, *13*, 24.
- [80] P. Xi, B. Huang, J. Yin, J. Jin, M. Lu, H. Zhang, Y. Peng, C. H. Yan, *J. Am. Chem. Soc.* **2020**, *142*, 18378.
- [81] P. Zhai, M. Xia, Y. Wu, G. Zhang, J. Gao, B. Zhang, S. Cao, Y. Zhang, Z. Li, Z. Fan, C. Wang, X. Zhang, J. T. Miller, L. Sun, J. Hou, *Nat. Commun.* **2021**, *12*, 4587.
- [82] Y. Xue, B. Huang, Y. Yi, Y. Guo, Z. Zuo, Y. Li, Z. Jia, H. Liu, Y. Li, *Nat. Commun.* **2018**, *9*, 1460.
- [83] Y. Shi, W. M. Huang, J. Li, Y. Zhou, Z. Q. Li, Y. C. Yin, X.-H. Xia, *Nat. Commun.* **2020**, *11*, 4558.
- [84] Z. Jin, A. J. Bard, *Proc. Natl. Acad. Sci. USA* **2020**, *117*, 12651.
- [85] Z. Zhang, C. Feng, X. Li, C. Liu, D. Wang, R. Si, J. Yang, S. Zhou, J. Zeng, *Nano Lett.* **2021**, *21*, 4795.
- [86] M. Tavakkoli, N. Holmberg, R. Kronberg, H. Jiang, J. Sainio, E. I. Kauppinen, T. Kallio, K. Laasonen, *ACS Catal.* **2017**, *7*, 3121.
- [87] L. Zhang, L. Han, H. Liu, X. Liu, J. Luo, *Angew. Chem., Int. Ed.* **2017**, *56*, 13694.
- [88] J. Zhang, Y. Zhao, X. Guo, C. Chen, C. L. Dong, R. S. Liu, C. P. Han, Y. Li, Y. Gogotsi, G. Wang, *Nat. Catal.* **2018**, *1*, 985.
- [89] J. Li, Q. Guan, H. Wu, W. Liu, Y. Lin, Z. Sun, X. Ye, X. Zheng, H. Pan, J. Zhu, S. Chen, W. Zhang, S. Wei, J. Lu, *J. Am. Chem. Soc.* **2019**, *141*, 14515.
- [90] N. Xuan, J. Chen, J. Shi, Y. Yue, P. Zhuang, K. Ba, Y. Sun, J. Shen, Y. Liu, B. Ge, Z. Sun, *Chem. Mater.* **2019**, *31*, 429.
- [91] K. Jiang, B. Liu, M. Luo, S. Ning, M. Peng, Y. Zhao, Y. R. Lu, T. S. Chan, F. M. F. de Groot, Y. Tan, *Nat. Commun.* **2019**, *10*, 1743.
- [92] Z. Wang, J. Yang, J. Gan, W. Chen, F. Zhou, X. Zhou, Z. Yu, J. Zhu, X. Duan, Y. Wu, *J. Mater. Chem. A* **2020**, *8*, 10755.
- [93] L. Zhang, J. M. T. A. Fischer, Y. Jia, X. Yan, W. Xu, X. Wang, J. Chen, D. Yang, H. Liu, L. Zhuang, M. Hankel, D. J. Searles, K. Huang, S. Feng, C. L. Brown, X. Yao, *J. Am. Chem. Soc.* **2018**, *140*, 10757.
- [94] Z. Wang, J. Yang, J. Cao, W. Chen, G. Wang, F. Liao, X. Zhou, F. Zhou, R. Li, Z. Q. Yu, G. Zhang, X. Duan, Y. Wu, *ACS Nano* **2020**, *14*, 6164.
- [95] G.-L. Hou, T. Yang, M. Li, J. Vanbuel, O. V. Lushchikova, P. Ferrari, J. M. Bakker, E. Janssens, *Angew. Chem., Int. Ed.* **2021**, *60*, 27095.
- [96] X. Mu, X. Gu, S. Dai, J. Chen, Y. Cui, Q. Chen, M. Yu, C. Chen, S. Liu, S. Mu, *Energy Environ. Sci.* **2022**, *15*, 4048.
- [97] Y. Han, Y.-G. Wang, W. Chen, R. Xu, L. Zheng, J. Zhang, J. Luo, R.-A. Shen, Y. Zhu, W.-C. Cheong, C. Chen, Q. Peng, D. Wang, Y. Li, *J. Am. Chem. Soc.* **2017**, *139*, 17269.
- [98] M. Zhu, C. Zhao, X. Liu, X. Wang, F. Zhou, J. Wang, Y. Hu, Y. Zhao, T. Yao, L. M. Yang, Y. Wu, *ACS Catal.* **2021**, *11*, 3923.
- [99] B. You, M. T. Tang, C. Tsai, F. Abild-Pedersen, X. Zheng, H. Li, *Adv. Mater.* **2019**, *31*, 1807001.
- [100] Y. Zheng, Y. Jiao, Y. Zhu, L. H. Li, Y. Han, Y. Chen, M. Jaroniec, S.-Z. Qiao, *J. Am. Chem. Soc.* **2016**, *138*, 16174.
- [101] E. J. Popczun, C. G. Read, C. W. Roske, N. S. Lewis, R. E. Schaak, *Angew. Chem., Int. Ed.* **2014**, *53*, 5427.
- [102] K. Xu, H. Ding, M. Zhang, M. Chen, Z. Hao, L. Zhang, C. Wu, Y. Xie, *Adv. Mater.* **2017**, *29*, 1606980.

- [103] M. W. Kanan, D. G. Nocera, *Science* **2008**, 321, 1072.
- [104] J. Yan, L. Kong, Y. Ji, J. White, Y. Li, J. Zhang, P. An, S. Liu, S.-T. Lee, T. Ma, *Nat. Commun.* **2019**, 10, 2149.
- [105] C. Feng, M. B. Faheem, J. Fu, Y. Xiao, C. Li, Y. Li, *ACS Catal.* **2020**, 10, 4019.
- [106] S. Sultan, J. N. Tiwari, A. N. Singh, S. Zhumagali, M. Ha, C. W. Myung, P. Thangavel, K. S. Kim, *Adv. Energy Mater.* **2019**, 9, 1900624.
- [107] N.-T. Suen, S.-F. Hung, Q. Quan, N. Zhang, Y.-J. Xu, H. M. Chen, *Chem. Soc. Rev.* **2017**, 46, 337.
- [108] Y.-C. Zhang, C. Han, J. Gao, L. Pan, J. Wu, X.-D. Zhu, J.-J. Zou, *ACS Catal.* **2021**, 11, 12485.
- [109] J. Wang, S.-J. Kim, J. Liu, Y. Gao, S. Choi, J. Han, H. Shin, S. Jo, J. Kim, F. Ciucci, H. Kim, Q. Li, W. Yang, X. Long, S. Yang, S.-P. Cho, K. H. Chae, M. G. Kim, H. Kim, J. Lim, *Nat. Catal.* **2021**, 4, 212.
- [110] L. C. Seitz, C. F. Dickens, K. Nishio, Y. Hikita, J. Montoya, A. Doyle, C. Kirk, A. Vojvodic, H. Y. Hwang, J. K. Nørskov, T. F. Jaramillo, *Science* **2016**, 353, 1011.
- [111] Y. Yao, S. Hu, W. Chen, Z.-Q. Huang, W. Wei, T. Yao, R. Liu, K. Zang, X. Wang, G. Wu, W. Yuan, T. Yuan, B. Zhu, W. Liu, Z. Li, D. He, Z. Xue, Y. Wang, X. Zheng, J. Dong, C.-R. Chang, Y. Chen, X. Hong, J. Luo, S. Wei, W.-X. Li, P. Strasser, Y. Wu, Y. Li, *Nat. Catal.* **2019**, 2, 304.
- [112] N. Danilovic, R. Subbaraman, K. C. Chang, S. H. Chang, Y. Kang, J. Snyder, A. P. Paulikas, D. Strmcnik, Y. T. Kim, D. Myers, V. R. Stamenkovic, N. M. Markovic, *Angew. Chem., Int. Ed.* **2014**, 53, 14016.
- [113] J. Zhou, L. Zhang, Y.-C. Huang, C.-L. Dong, H.-J. Lin, C.-T. Chen, L. H. Tjeng, Z. Hu, *Nat. Commun.* **2020**, 11, 1984.
- [114] J. Nai, Y. Lu, L. Yu, X. Wang, X. W. Lou, *Adv. Mater.* **2017**, 29, 1703870.
- [115] J. Yu, F. A. Garcés-Pineda, J. González-Cobos, M. Peña-Díaz, C. Rogero, S. Giménez, M. C. Spadaro, J. Arbiol, S. Barja, J. R. Galán-Mascarós, *Nat. Commun.* **2022**, 13, 4341.
- [116] Y. P. Zhu, C. Guo, Y. Zheng, S.-Z. Qiao, *Acc. Chem. Res.* **2017**, 50, 915.
- [117] S. Li, Y. Gao, N. Li, L. Ge, X. Bu, P. Feng, *Energy Environ. Sci.* **2021**, 14, 1897.
- [118] a) J. Kibsgaard, I. Chorkendorff, *Nat. Energy* **2019**, 4, 430; b) Y. Wang, D. Wang, Y. Li, *Adv. Mater.* **2021**, 33, 2008151.
- [119] C. C. L. McCrory, S. Jung, I. M. Ferrer, S. M. Chatman, J. C. Peters, T. F. Jaramillo, *J. Am. Chem. Soc.* **2015**, 137, 4347.
- [120] J. Shan, C. Ye, S. Chen, T. Sun, Y. Jiao, L. Liu, C. Zhu, L. Song, Y. Han, M. Jaroniec, Y. Zhu, Y. Zheng, S.-Z. Qiao, *J. Am. Chem. Soc.* **2021**, 143, 5201.
- [121] Y. Jiao, Y. Zheng, M. Jaroniec, S. Z. Qiao, *Chem. Soc. Rev.* **2015**, 44, 2060.
- [122] B. H. R. Suryanto, Y. Wang, R. K. Hocking, W. Adamson, C. Zhao, *Nat. Commun.* **2019**, 10, 5599.
- [123] B. You, Y. Sun, *Adv. Energy Mater.* **2016**, 6, 1502333.
- [124] B. You, N. Jiang, M. Sheng, S. Gul, J. Yano, Y. Sun, *Chem. Mater.* **2015**, 27, 7636.
- [125] B. You, N. Jiang, M. Sheng, M. W. Bhushan, Y. Sun, *ACS Catal.* **2016**, 6, 714.
- [126] Q. Wang, C.-Q. Xu, W. Liu, S.-F. Hung, H. Bin Yang, J. Gao, W. Cai, H. M. Chen, J. Li, B. Liu, *Nat. Commun.* **2020**, 11, 4246.
- [127] B. You, Y. Zhang, Y. Jiao, K. Davey, S. Z. Qiao, *Angew. Chem., Int. Ed.* **2019**, 58, 11796.
- [128] J. Kibsgaard, T. F. Jaramillo, *Angew. Chem., Int. Ed.* **2014**, 53, 14433.
- [129] K. Kodama, T. Nagai, A. Kuwaki, R. Jinnouchi, Y. Morimoto, *Nat. Nanotechnol.* **2021**, 16, 140.
- [130] M. D. Allendorf, *Nat. Energy* **2016**, 1, 16058.
- [131] M. K. Debe, *Nature* **2012**, 486, 43.
- [132] H. T. Chung, D. A. Cullen, D. Higgins, B. T. Sneed, E. F. Holby, K. L. More, P. Zelenay, *Science* **2017**, 357, 479.
- [133] S. Zaman, L. Huang, A. I. Douka, H. Yang, B. You, B. Y. Xia, *Angew. Chem., Int. Ed.* **2021**, 60, 17832.
- [134] T. Ioroi, Z. Siroma, S. Yamazaki, K. Yasuda, *Adv. Energy Mater.* **2019**, 9, 1801284.
- [135] Z. Wang, X. Jin, C. Zhu, Y. Liu, H. Tan, R. Ku, Y. Zhang, L. Zhou, Z. Liu, S.-J. Hwang, H. J. Fan, *Adv. Mater.* **2021**, 33, 2104718.
- [136] a) M. A. Bajada, J. Sanjosé-Orduna, G. D. Liberto, S. Tosoni, G. Pacchioni, T. Noël, G. Vilé, *Chem. Soc. Rev.* **2022**, 51, 3898; b) G. Vilé, D. Albani, M. Nachtegaal, Z. Chen, D. Dontsova, M. Antonietti, N. López, J. Pérez-Ramírez, *Angew. Chem., Int. Ed.* **2015**, 54, 11265; c) D. M. Weekes, D. A. Salvatore, A. Reyes, A. Huang, C. P. Berlinguette, *Acc. Chem. Res.* **2018**, 51, 910.
- [137] a) G. Vilé, D. Ng, Z. Xie, I. Martínez-Botella, J. Tsanaktsidis, C. H. Hornung, *ChemCatChem* **2022**, 14, 202101941; b) K. Lan, D. Zhao, *Nano Lett.* **2022**, 22, 3177; c) D. Wang, Y. Zou, L. Tao, Y. Zhang, Z. Liu, S. Du, S. Zang, S. Wang, *Chin. Chem. Lett.* **2019**, 30, 826.
- [138] L. Cao, X. Liu, X. Shen, D. Wu, T. Yao, *Acc. Chem. Res.* **2022**, 55, 2594.
- [139] J. Yang, W. Liu, M. Xu, X. Liu, H. Qi, L. Zhang, X. Yang, S. Niu, D. Zhou, Y. Liu, Y. Su, J.-F. Li, Z.-Q. Tian, W. Zhou, A. Wang, T. Zhang, *J. Am. Chem. Soc.* **2021**, 143, 14530.
- [140] B. Pattengale, Y. Huang, X. Yan, S. Yang, S. Younan, W. Hu, Z. Li, S. Lee, X. Pan, J. Gu, J. Huang, *Nat. Commun.* **2020**, 11, 4114.
- [141] a) J. Shan, C. Ye, Y. Jiang, M. Jaroniec, Y. Zheng, S.-Z. Qiao, *Sci. Adv.* **2022**, 8, eabo0762; b) T. Sun, S. Mitchell, J. Li, P. Lyu, X. Wu, J. Pérez-Ramírez, J. Lu, *Adv. Mater.* **2021**, 33, 2003075.
- [142] R. Zhao, X. Yue, Q. Li, G. Fu, J.-M. Lee, S. Huang, *Small* **2021**, 17, 2100391.
- [143] J. Zheng, W. Sheng, Z. Zhuang, B. Xu, Y. Yan, *Sci. Adv.* **2022**, 2, e1501602.
- [144] E. S. Davydova, S. Mukerjee, F. Jaouen, D. R. Dekel, *ACS Catal.* **2018**, 8, 6665.
- [145] L. An, X. Zhao, T. Zhao, D. Wang, *Energy Environ. Sci.* **2021**, 14, 2620.
- [146] P. Yang, J.-M. Tarascon, *Nat. Mater.* **2012**, 11, 560.



Bo You received his Ph.D. degree in 2014 under the supervision of Prof. Zhaoxiang Deng at University of Science and Technology of China (USTC). He joined Prof. Yujie Sun's group at Utah State University, where he worked from 2014 to 2016, then Prof. Hong Li's group at Nanyang Technological University from 2016 to 2017, and then Prof. Shi Zhang Qiao's group at The University of Adelaide from 2017 to 2019 as a postdoctoral researcher. Currently, he is a full professor at Huazhong University of Science and Technology (HUST). His research focuses on integration-designed electro-activation (IDEA) for advanced renewable energy.